Control of crustal strength, tectonic inheritance and extrusion/indentation rates on crustal deformation and basin reactivation: insights from laboratory models

Benjamin Guillaume[1], Guido M. Gianni[2,3], Jean-Jacques Kermarrec[1], and Khaled Bock[1]

[1]University of Rennes, CNRS, Géosciences Rennes, UMR 6118, Rennes, France
[2]Consejo Nacional de Investigaciones Científicas y Técnicas (CONICET)
[3]Instituto Geofísico Sismológico Ing. Fernando Volponi (IGSV), Universidad Nacional de San Juan. San Juan, Argentina

Correspondence: Benjamin Guillaume (benjamin.guillaume@univ-rennes1.fr)

Abstract. Geological settings characterized by the simultaneous action of multiple tectonic regimes provide a unique opportunity to understand complex interactions among different geodynamic processes. From an experimental point of view, these contexts remain comparatively less studied than areas with more simple patterns of deformation resulting from primary plate-boundary interactions. Here, we carried out analog experiments involving simultaneous shortening and orthogonal extension

5 under different rheological conditions, and including the effect of crustal inheritance. We performed brittle experiments and brittle-ductile experiments to simulate cases of "strong" and "weak" crusts, respectively. We present two types of experiments: i) one stage experiments with either shortening-only or synchronous orthogonal shortening and stretching, and ii) two stages experiments with a first phase of stretching and a second phase with either shortening-only or synchronous orthogonal shortening and stretching. In our models, deformation occurs by a combination of normal, thrust, and strike-slip faults with

10 structures location depending on boundary conditions and crustal inheritance. For brittle models, we show that the three types of structures can develop at the same time for intermediate ratios of extrusion over indentation rates ($1.4 < V_e/V_s < 2$). For brittle-ductile models, we observe either shortening-orthogonal thrust faults associated with conjugate strike-slip faults (models with low V_e/V_s and no initial extensional phase) or stretching-orthogonal normal faults associated with conjugate strike-slip faults (models with high V_e/V_s and initial extensional phase). Whatever the crustal strength, the past deformation history,

15 and the extrusion/indentation ratio, both normal and thrust faults remain with similar orientations, i.e. stretching-orthogonal and shortening-orthogonal, respectively. Instead, strike-slip faults exhibit variable orientations with respect to the indentation direction, which may be indicative of the strength of the crust and/or of the extrusion/indentation ratio. We also show that extensional structures formed during a first stage of deformation are never inverted under orthogonal shortening but can be reactivated as normal or strike-slip faults depending on V_e/V_s. The models replicate some deformation patterns documented in

20 nature. Independently of the crustal rheology or the presence of crustal weaknesses, conjugate strike-slips faults develop along with variable normal faulting during compression/indentation, reminiscent of tectonic escape processes along the Himalayas-Alpine chain.

1 Introduction

Primary interactions at plate boundaries and the derived stress fields result in tectonic regimes characteristics of different
geodynamic settings (e.g., Anderson, 1905). For instance, contractional regimes are more common in convergent margins in
non-collisional (e.g., Central Andes, Barnes and Ehlers (2009)) and collisional orogens (e.g., Tibetan orogenic Plateau, Royden
et al. (2008)) associated with fold-and-thrust belt development and crustal thickening. Extensional regimes are characteristic
of divergent margins associated with mid-ocean ridges, intraplate regions in continental rifts (e.g., East African rift system,
Chorowicz (2005); Basin and Range Province, Dickinson (2002)), and retreating subduction settings in intra-arc and backarc
areas (e.g., Western Pacific marginal basins, Hilde et al. (1977)). Strike-slip regimes can be found in convergent settings where
transcurrent faults run along magmatic arcs in contexts of oblique subduction (e.g., Liquiñe-Ofqui fault zone, Cembrano et
al. (1996); the Great Sumatra fault, Berglar et al. (2010); Median Tectonic Line in Japan, Takagi (1986)), in hinterland
regions of collisional orogens and related areas of tectonic escape (Tapponnier et al. , 1982, 2001), in intraplate transcurrent
regions (Molnar and Dayem , 2010), and at plate-boundary transform zones (e.g., Woodcock , 1986). In all settings, upper-
plate weaknesses exert a major control in nucleation, reactivation, and orientation of structures (e.g., Sutherland et al. , 2000;
Tapponnier et al. , 2001; Chorowicz , 2005; Pfiffner , 2017). Noteworthy, the three tectonic regimes can take place variably in
all geodynamic settings, and at any one time during deformation, contrasting regimes may be active at different places (e.g.,
Harland and Bayly , 1958; Woodcock , 1986; Zoback , 1992). Cases where multiple tectonic regimes acted closely in space
and time have long been recognized. The coexistence of thrust, strike-slip, and normal faulting has been documented in thick
orogenic regions reaching crustal thicknesses above ∼60 km (e.g., Molnar and Tapponnier , 1978; Giambiagi et al. , 2016),
in oblique convergent settings associated with strain partitioning (Chemenda et al. , 2000), in areas of indentation tectonics
and lateral escape (Tapponnier et al. , 1982, 2001; Scharf et al. , 2013), and synorogenic foreland rifting/transtension settings,
where extension-transtension takes place in close spatiotemporal relation with plate-margin shortening (Sengör , 1976; Dèzes
et al. , 2004; Gianni et al. , 2015). However, the mechanisms allowing the coeval existence of different tectonic regimes are not
yet fully understood.

From a modeling point of view, numerical and analog models have been helpful to gain insights into the kinematic and
dynamic evolution of geological structures associated with contractional (e.g., Davis et al. , 1983; Koyi , 1995; Burbidge and
Braun , 2002; Lohrmann et al. , 2003; Simpson , 2011; Graveleau et al. , 2012), extensional (e.g., Vendeville et al. , 1987; Brun
, 1999; Zwaan et al. , 2016), and strike-slip regimes (e.g., McClay and Bonora , 2001; Dooley and Schreurs , 2012). These
studies allowed a better understanding of deformation at crustal or lithospheric scale and basin-formation processes simulating
scenarios that reproduce a particular tectonic regime or a succession of these, such as in basin inversion experiments (e.g.,
Buiter and Pfiffner , 2003; Bonini et al. , 2012). Comparatively less efforts have been devoted to reproduce more complex
scenarios, where several tectonic regimes acted in concert producing intricate patterns of deformation. Pioneering lithospheric-
scale analog studies have aimed to replicate regional deformation associated with shortening, strike-slip, and extension in
the eastern Asian lithosphere triggered by the collisional far-field effects of India (e.g., Tapponnier et al. , 1982; Davy and
Cobbold , 1988; Fournier et al. , 2004). Similarly, brittle-ductile analog and 3-D numerical experiments have been applied

to understand complex regional deformation resulting from the close interrelation between the indentation of Arabia, lateral escape of Anatolia, and backarc extension in the Aegean region (e.g., Martinod et al. , 2000; Sternai et al. , 2014) and lateral escape and extension in the eastern Alps resulting from the indentation of the Adriatic plate (Ratschbacher et al. , 1991). More

60 recently, Dhifaoui et al. (2021) analyzed through brittle-ductile analog models a case study of simultaneous compression and lateral extension at the eastern boundary of the North African Alpine Chain, where coexisting graben, strike-slip, and thrusts faults formed a complex structural pattern in the general context of Nubia-Eurasia plates convergence. While these studies provide some elements for understanding the co-existence of different tectonic regimes and associated structures, there is a lack for a systematic investigation of the role of the relative ratio between shortening and stretching rates, as horizontal

65 extrusion may not always only result from orthogonal indentation. In addition, the role of the strength of the crust, owing to its composition or to inherited structures, is not always taken into account, while it may be of importance in controlling the type and location of structures accommodating deformation (e.g., Munteanu et al. , 2013; Zwaan et al. , 2021).

In this study, we carry out a series of brittle and brittle-ductile analog experiments to gain insights into the role played by simultaneous shortening and orthogonal extension under different boundary and rheological conditions on the crustal tectonic

70 regime. We also analyze the role of crustal inheritance on fault reactivation and potential basin inversion during coeval shortening and lateral extension, which has not been explored so far. Although we do not intend to reproduce any specific natural case, we find some similarities between our experiments and deformation patterns in several natural cases, which provide additional insights into the rheological conditions and kinematics associated with their formation.

2 Laboratory models

75 2.1 Materials

We perform both brittle (one-layer) experiments (models BI) and brittle-ductile (two-layers) experiments (models CE) to reproduce a brittle upper crust and a brittle-ductile crust simulating cases of "strong" and "weak" crusts, respectively (Fig. 1). For both types of experiments, the 4-cm thick single or double layers rest on top of a foam layer (8-cm thickness). To simulate the brittle part of the crust, whose behaviour is of Mohr–Coulomb type (Byerlee , 1978), we use the Fontainebleau

80 quartz sand (NE34, Sibelco, France, D50 = 210 μm) (Klinkmüller et al. , 2016). This material has a peak friction of 0.74 and an immediate reactivation friction (after 10 s) of 0.64. Healing of this material increases the reactivation friction to 0.68 after 2.6 hours (maximum duration of our experiments) (Table 1). The cohesion of Fontainebleau quartz sand is around 60-70 Pa. We sieve the dry sand from a height of ∼15-20 cm, ensuring that its density is 1400 kg/m^3. Dry sand exhibits frictional plastic behaviour, and the geometry of structures that form when deformed does not depend on the applied strain rate.

85 To simulate the ductile part of the crust, we use PDMS silicone whose density is 965 kg/m^3 and viscosity μ is around 3.5 × 10^4 Pa s. This material has a Newtonian rheology (n=1) for strain rates lower than 10^{-2} s^{-1} (e.g., Rudolf et al. , 2016; Guillaume et al. , 2021), which is the case in our study where imposed strain rates are in the range 1.2-4.5x10^{-5} s^{-1}. The

strength of the layer of silicone putty ($\sigma_1 - \sigma_3$) varies with imposed strain rates as:

$$\sigma_1 - \sigma_3 = \eta\dot{\epsilon} \tag{1}$$

90   where η is the viscosity and $\dot{\epsilon}$ the strain rate. For the values of applied strain rates, differential stress is on the order of 0.4-1.6 Pa. Initial strength enveloppes for both types of models and different parts of the models are shown in Fig. 1. The foam used at the base of the model has a Poisson coefficient of 0.12 and allows producing a linearly varying velocity field (no velocity discontinuities) at the base of the deforming pile by compressing it to obtain shortening or letting it decompress to obtain stretching. However, there is a limitation on the amount of applied stretching/shortening. After 20% of shortening, the foam

95   starts buckling and we therefore limit the amount of applied stretching/shortening under this threshold.

2.2 Scaling

We follow the scaling procedure shown e.g., in Zwaan et al. (2019) and based on Hubbert (1937); Ramberg (1981); Weijermars and Schmeling (1986). The scaling parameters are given in Table 2. Stress ratios between the laboratory and nature σ^* are calculated as follows:

100    $$\sigma^* = \rho^* g^* L^* \tag{2}$$

where ρ^* represents the density ratio, g^* the gravity ratio, and L^* the length ratio. Considering that we simulate the upper 15 km of the crust with our 4-cm thick pile of material, it gives $\sigma^* = 1.33\ 10^{-6}$, i.e. that 1 Pa in the lab corresponds to 0.75 MPa in nature.

One may notice that for the two-layered models, the density ratio between the brittle and ductile parts of the crust is high

105   (1.45), leading to buoyancy forces that may trigger gravitational instability of the silicone layer and possible diapirism. However, given the relatively high viscosity of the silicone layer and the short duration of these models (between 1.6 and 2.6 h), such process may remain limited during the experimental time frame.

The strain rate ratio $\dot{\epsilon}^*$ is obtained as the ratio between the stress ratio σ^* and the viscosity ratio η^*:

$$\dot{\epsilon}^* = \sigma^*/\eta^* \tag{3}$$

110   We assume a natural viscosity for the crust of 10^{21} Pa.s, within the range of proposed values under varying tectonic contexts ($\eta = 10^{19}\text{-}10^{23}$ Pa.s; (e.g., Buck , 1991; Brun , 1999; Bürgman and Dresen , 2008)). It gives $\dot{\epsilon}^* = 3.8\ 10^{10}$, i.e. imposed strain rates correspond to strain rates of $0.32\text{-}1.18\text{x}10^{-15}$ s^{-1} in nature.

The time ratio t^* can be obtained from:

$$\dot{\epsilon}^* = 1/t^* \tag{4}$$

115   It implies that 1h in the lab corresponds to 4.34 Ma in nature. Given that the duration of our models is at maximum 2.6 h, we simulate geological processes lasting for $\sim$11 Ma at maximum.

The velocity ratio v^* is obtained from:

$$\dot{\epsilon}^* = v^*/L^* \tag{5}$$

The imposed values for extension/shortening rates between 0 and $\sim$60 mm/h in the lab corresponds to 0-5.2 mm/yr in
120 nature, typical values for continental rifting (e.g., Saria et al. , 2014), subduction-related (e.g., Andes,Oncken et al. (2006);
Alps, Sternai et al. (2019); Zagros, Tatar et al. (2002)) or intra-continental collision orogens (e.g., Pyrenees, Mouthereau et
al. (2014); Tian Shan, Saint-Carlier et al. (2016)).

The dynamic similarity between our experiments and the natural case for the viscous regime is verified by computing the
ratio between lithostatic pressure and viscous strength (Ramberg number R_m):

125 $$R_m = (\rho g L^2)/(\eta v) \tag{6}$$

which gives a value of $\sim$37 considering the maximum deformation velocity for both the model and the natural case. For the
brittle regime, the dimensionless friction coefficient is similar (0.6-0.7) in the laboratory and in nature. A similar ratio between
gravitational stress and cohesive strength $R_s = \rho g L/C$ is achieved considering a cohesion in nature of 45-52 MPa, which is
well within the range of cohesion values measured on natural rocks at 24-110 MPa (Jaeger and Cook , 1976; Raleigh and
130 Paterson , 1965; Twiss and Moore , 1992; Handin , 1969).

2.3 Procedure and analysis

The 60 x 60 x 8 cm layer of foam is initially compressed in one direction and is maintained in this state for the rest of the
preparation phase. For the two-layers models, we place a pre-cut silicone plate with dimensions of 50 cm x 50 cm x 2 cm.
Seeding of the sand is performed by depositing it from a distance of $\sim$15-20 cm and leveling it with a rigid plate until the
135 desired thickness is achieved. The brittle part of the crust is made of white quartz sand that is randomly sprinkled on top with
black colored sand in order to allow particles detection for digital image correlation. Before deformation, the models cover an
area of ca. 46 cm x 46 cm that would represent an area of 172 km x 172 km in nature.

We also include "seeds" in our models to help localizing deformation. They may represent weak zones inherited from
previous phases of deformation. These seeds are linear pieces of silicone that are placed on top of the silicone layer, or directly
140 on top of the foam for the brittle models (Fig. 1). They are placed at the center of the models, orthogonal to the extension
direction, have a rectangular shape and extend on the entire length of the model. The dimensions of the seed are 46 cm x 1.5
cm x 1.5 cm for the brittle-ductile models and 46 cm x 1.5 cm x 1 cm for the brittle models (Fig. 1). The strength of the crust
is decreased at these locations owing to the reduced thickness of the overlying sand layer (Fig. 1), which in turn may help
deformation to localize. The layer(s) are then deformed by applying a constant velocity boundary condition at the edges of
145 the model through pistons controlled by step motors. Stretching (extrusion) is applied on both edges of the models by letting
the foam decompress while shortening (indentation) is only applied at one side of the models, the other side having a no-
motion boundary condition (Fig. 1). We arbitrary consider the non-moving wall as the north in our experiments. We performed
two types of experiments: i) one stage experiments with either shortening-only or synchronous orthogonal shortening and

stretching, and ii) two stages experiments with a first phase of 5% stretching and a second phase with either shortening-only or
150 synchronous orthogonal shortening and stretching, in order to study the possible reactivation/inversion of structures (Fig. 2).

We do not include surface processes in the models (erosion, deposition), especially in between the two phases of deformation, meaning that the created grabens remain unfilled when the second phase of deformation starts. While we acknowledge that redistribution of mass associated with surface processes may impact stress distribution and further deformation (e.g., Mugnier et al. , 1997; Pinto et al. , 2010) we wanted to ensure similar conditions between models that are difficult to achieve when
155 manually intervening during the course of the experiment.

Experiments are recorded from the top by a DSLR camera taking pictures every 2 minutes. Pictures are then automatically analyzed using an image cross-corelation technique, Particle Image velocimetry (PIV), using the PIVlab software (Thielicke and Sonntag , 2021). We pre-process the images with a CLAHE filter with a window size of 64 px to enhance contrast in the pictures and allow particles detection. PIV analyses are made with the FFT window deformation PIV algorithm in 3 passes
160 with interrogation areas of 128, 64, and 32 pixels, and with a step of 50%. PIV results are then calibrated using spatial scales set on top of the models. We obtain velocity maps with a spatial resolution of 16 pixels, corresponding to ∼4 mm (∼1.5 km in nature).

Velocity fields obtained from the PIV analyses are then processed with the strain map algorithm (Broerse et al. , 2021) that allows tracking the cumulative deformation field and as such to map the distribution of deformation over time. In particular this
165 algorithm based on the description of shape changes in terms of Hencky strains allows to discriminate co-existing strike-slip faults, thrust faults and normal faults, and their evolution over time, and as such efficiently complement inherently subjective visual inspection. Videos and strain analysis of the twelve experiments are available in Guillaume et al. (2022).

3 Results

3.1 Brittle-only models: role of inheritance under varying stress fields

170 #### 3.1.1 Inheritance as a crustal heterogeneity (seed)

We investigate the role of a crustal heterogeneity (basal seed orthogonal to the stretching direction) on deformation location under different kinematic boundary conditions. For this, we performed a series of five models in which the ratio of stretching velocity (extrusion rate) over shortening velocity (indentation rate) V_e/V_s is varied between 0 (no stretching) and 2.8 (stretching dominated). We compute the principal stretches λ_{max} and λ_{min} and the corresponding strain type for the five models after 4%
175 of shortening (SM1) and 10% of stretching (Fig. 3).

For the model with shortening-only (BI10), deformation is first concentrated along a E-W striking thrust fault located ∼10 cm from the moving piston. The thrust has a linear shape, orthogonal to the shortening direction. Increase in the amount of shortening leads to the activation of three successive thrusts in a prograde sequence.

For the model with $V_e/V_s = 0.9$ (BI09), deformation is also mainly accommodated by E-W thrust faults developing in a
180 prograde sequence. However, unlike the previous model, the shape of the thrust front is not linear but rather convex toward

the north. In this model, deformation is also accommodated by N-S extensional faults located close to the edges of the model. There are no traces of significant extension above the central seed.

For the model with V_e/V_s = 1.4 (BI05), after 4% of shortening (5.5% of stretching), deformation is partitioned between shortening that is accommodated along an E-W thrust fault, diffuse extension in the retrowedge, and strike-slip faults at the corners of the model (Fig. SM1). After 10% of stretching (7.7% of shortening), the pattern of deformation has evolved with: i) stretching in the center of the model accommodated by N-S conjugate normal faults forming a 5.2-cm large graben structure, ii) shortening accommodated by a second thrust fault, and iii) conjugate strike-slip structures that make the connection between the frontal thrust and the central graben, but also that deform the southern wedge. In the distal part of the retrowedge, other strike-slip faults are visible with a sense of shear that is compatible with previous strike-slip faults but with orientations that largely differ (N66 and N114 in the northern sector vs. N25-N40 and N145-N150 in the south central sector) (Fig. 3).

For the model with V_e/V_s = 1.9 (BI06), the N-S striking central graben is already formed after 4% of shortening (7.6% of stretching) and deformation is also localized along conjugate strike-slip faults. Instead, shortening is not accommodated by discrete E-W thrust faults but rather correspond to a zone of diffuse deformation. After, 10% of stretching (5.1% of shortening), the normal faults remain active and strike-slip faults propagate toward the central graben. Like in the model BI05, a transition zone with strike-slip faults develop in between the wedge and the central graben.

For the model with V_e/V_s = 2.8 (BI07), the evolution of deformation is almost similar to the previous experiment. The main difference is visible after 10% of extension: there are no strike-slip faults in the transition zone between the mildly shortened area and the central graben.

3.1.2 Inheritance as a former extensional phase

In the following models, the set-up is identical to previous models excepted that they undergo an initial phase of E-W extension with up to 5-5.3% of stretching, prior to a second phase of N-S shortening (and possible coeval E-W stretching). We test three kinematic boundary conditions for the second phase of deformation : V_e/V_s = 0 (BI01), V_e/V_s = 1.4 (BI08), V_e/V_s = 2 (BI11) (Fig. 4) that should be compared with models BI10, BI05, and BI06, respectively.

For model with V_e/V_s = 0, the first phase of stretching results in the development of N-S conjugate normal faults and an associated 5.3-cm large graben (Fig. 4). In the second phase of deformation with N-S shortening only, a first thrust develops. After 4% of shortening, deformation is accommodated along new thrusts. However, these thrusts do not cut through the entire width of the models like in model BI10 but rather branch on previous thrusts (Fig. 4). Interestingly, the intersections between the new and former thrusts are close, but not exactly coincide, to the limits of the downlifted central area.

For model with V_e/V_s = 1.4, the first phase of extension also results in the formation of a central N-S striking graben, similar to model BI01. However, in the second phase of deformation, deformation is accommodated by the coeval activity of N-S normal faults, an E-W thrust fault and NW-SE and NE-SW conjugate strike-slip faults that develop in the wedge, at the transition between the frontal thrust and the central graben and at the northern boundary of the model. The pattern of deformation differs from model BI05 in that after the same amount of shortening, localization of extensional structures and strike-slip faults was not achieved. It is only afer 10% of extension that the overall pattern of deformation appears almost

215 similar. However, second-order differences remain: i) the shape of the frontal thrust is convex toward the north in the model
with an initial phase of stretching, ii) the strike-slip faults that develop in the wedge have orientations that slightly differs: N55
(sinistral) and N120 (dextral) in model BI08 instead of N40 and N140 in model BI05.

For model with V_e/V_s = 2, stretching dominates in the model and is accommodated through N-S normal faults, whose
activity pursues during the second phase of deformation (Figs. 4 and 5). Evidences of significant shortening localization are
220 lacking, but the experiment stopped after only 2.2% of shortening. The imposed kinematic boundary conditions also resulted
in the development of conjugate strike-slip faults at the southern and northern boundaries of the model.

3.2 Brittle-ductile models: role of inheritance under varying stress fields

3.2.1 Inheritance as a crustal heterogeneity (seed)

The model CE16 has been performed to test how the deformation distribution evolves as a function of the strength of the
225 crust, by including a ductile layer in the model. It is comparable with brittle-only model BI09, which shares similar boundary
conditions (V_e/V_s =0.9). After 4% of shortening (and 2.8% of stretching), deformation is accommodated by a combination of
diffuse shortening along a 4-cm large E-W band (Fig. 6) and conjugate strike-slip faults at the corners of the models. Unlike
model BI09, there are no N-S normal faults at this stage. After an amount of 10% of stretching (and 14.2% of shortening), the
area of diffuse shortening has evolved into a localized thrust fault. In addition, N-S shortening is also accommodated along
230 another thrust with northward dipping, forming an uplifted wedge.

3.2.2 Inheritance as a former extensional phase

The model CE17 is similar to model CE16 excepted that we impose an initial phase of 4.7% E-W stretching. This first phase
of stretching results in the localisation of strain along three pairs of N-S trending conjugate normal faults: one in the western
part of the model, one in the eastern part of the model and the last one in the central part of the model, located just above the
235 seed (Fig. 7). During the second phase of deformation with coeval shortening and stretching (V_e/V_s =0.9), some of the pre-
existing normal faults are reactivated as normal faults, other as shortening-parallel strike-slip faults, while additional conjugate
strike-slip faults develop and branch at the corner of the models (Figs. 7 and 8). Increase in the amount of shortening does not
lead to significant localisation of deformation on reverse faults but rather leads to the development of new strike-slip faults.
The brittle-only model whose boundary conditions are the closest to model CE17 is model BI08. Despite a larger V_e/V_s ratio
240 in model BI08 that would favor stretching over shortening, the brittle-only model exhibits a clear E-W thrust fault that is not
observed in the brittle-ductile model.

Models CE18 and CE20 share a similar set-up with CE17 but explore different boundary conditions during the second phase
of deformation with V_e/V_s = 0.7 and V_e/V_s =1.1, respectively. We describe deformation after 5% of stretching during the
second phase of deformation (Fig. 9). For the model dominated by shortening (CE18), the two main differences with model
245 CE17 are i) the largest extent of zones characterized by diffuse shortening (Fig. 9) that maintains during the entire second phase
of deformation (Fig. 8) and ii) the limited sections of pre-existing normal faults that are reactivated as normal faults , which

only apply to a restricted area over the central seed. In addition, in the eastern part of the model one of the N-S normal faults is reactivated as a dextral strike-slip fault. For the model dominated by stretching (CE20), the pattern of deformation is clearly different: large portions of the pre-existing western, eastern and central normal faults are reactivated as normal faults during
250 the second phase of deformation. Only in the central portions of the western and central faults deformation is accommodated along strike-slip faults that are aligned with the initial orientation of normal faults (point b in Fig. 8).

4 Discussion

4.1 Tectonic regime distribution under non plane-strain conditions

Our models confirm that under plane-strain conditions, i.e. no strain in one of the horizontal directions (models BI01, BI10 and
255 first stage of models BI08, BI11, CE17, CE18, and CE20), the crust accommodates deformation through structures orthogonal to the direction of transport, i.e. either normal faults when the maximum principal stress (σ_1) is vertical or thrust faults when the minimum principal stress (σ_3) is vertical. However, when boundary conditions satisfy non plane-strain conditions (i.e. strain occurs along the three principal axis), deformation is accommodated along a combination of normal faults, thrusts faults and strike-slip faults, whose location and presence/absence appear to depend on the applied boundary conditions and pre-existing
260 heterogeneities.

In model BI05 for instance (brittle model with V_e/V_s = 1.4), the three modes of deformation are active at the same time with combined N-S conjugate normal faults, W-E thrust faults, and NE-SW and NW-SE conjugate strike-slip faults (Fig. 10). Interestingly, in the center of the model, the change of deformation mode is progressive from extensional structures to the north toward compressional structures to the south. An analysis of the stress state suggests that different tectonic regimes are
265 found within the model: extensional tectonic regime where σ_1 is vertical, wrench (strike-slip) regime where σ_2 is vertical and compression regime where σ_3 is vertical (Anderson, 1905). The transition from one regime to another therefore results from the permutation of one of the horizontal principal stress axes with the vertical one, controlled by the relative magnitude between the principal stresses as described by $b = (\sigma_2 - \sigma_3)/(\sigma_1 - \sigma_3)$. A change from extensional to wrench regime is favored for high b values while a change from wrench regime to compression regime is favored for low b values. The Mohr-Coulomb analysis
270 for a frictional material like sand also implies that the differential stress necessary for material failure is maximum for thrust faults (Fig. 10). This could explain why thrusts faults are only found close to the southern moving piston where the maximum horizontal stress is applied (zone 3). In this area, σ_1 is horizontal and N-S oriented, while the minimum stress (σ_3) is vertical. Going further north from the piston (zone 2), σ_1 is still N-S oriented but its magnitude decreases, which requires σ_3 to be lower when the material fails. As a consequence, the intermediate principal stress (σ_2) becomes vertical favoring the development of
275 strike-slip faults. Further north (zone 1), the normal faults that were created during the first phase of extension are reactivated as normal faults, thus indicating that the principal stress that is oriented in the N-S direction is no more σ_1 but σ_2, and that in turn σ_1 is vertical.

For brittle models, the coexistence of the three types of structures is only possible for intermediate V_e/V_s ratios (1.4< V_e/V_s <2). For lower V_e/V_s, σ_1 is horizontal and N-S oriented close to the piston applying shortening, favouring the development of

280 thrust sequences in the southern part of the models. Close to the western and eastern pistons applying stretching, in the case where $V_e/V_s \neq 0$, the vertical stress becomes the maximum stress and N-S normal faults develop. For values of $V_e/V_s \geq 2$, the W-E horizontal stress is low enough in the entire model to maintain as the minimum stress σ_3, which in turn implies that even if the N-S horizontal stress is the maximum stress σ_1, the crust cannot fail along E-W thrust faults, but fail along strike-slip faults.

285 For brittle-ductile models, over the range of tested V_e/V_s, we do not observe the coexistence of the three types of structures within the same model. We only observe E-W thrust faults associated with conjugate strike-slip faults for models with low V_e/V_s and no initial E-W extensional phase. This implies that the conditions where both horizontal E-W stress is low enough to become σ_3 and the vertical stress high enough to become σ_1 are never satisfied in the model. The first condition is met as testified by the presence of strike-slip faults. Instead, the second condition is not met, which could partly be explained 290 by the limited thickness of the brittle portion of the crust, which is half that of the brittle-only models. For models with an initial E-W extensional phase, we observe at the final stage of deformation a combination of N-S normal faults and conjugate strike-slip faults, and no clear W-E thrust faults, even when V_e/V_s is low. For the latter, shortening is active in some areas of the model (Fig. 9) but does not localize along discrete structures. For weak crusts, crustal thinning associated with an initial phase of extension therefore appear to control the future development of thrusts during subsequent phase of combined 295 shortening/stretching. However, the amount of applied deformation remains limited with only 5% of horizontal E-W stretching (and ∼10% of horizontal N-S shortening) and we cannot preclude that further shortening would eventually result in thrust development.

4.2 Compatibility of the structures with principal stresses orientation

In the brittle-only models, a majority of the structures are consistent with the Coulomb fracture criterion considering either a 300 N-S oriented horizontal σ_1 or a W-E oriented horizontal σ_3. In particular, thrust faults are W-E oriented, normal faults N-S oriented and strike-slip faults generally oriented at ∼30° from a N-S σ_1. However, in the northern part of the models, strike-slip faults do not obey this criterion and exhibit larger angles with respect to a N-S horizontal σ_1, with values around 60-70° (e.g., model BI05, Figs. 3 and 11). These anomalous strike-slip faults are directed toward the northward termination of the normal faults bounding the central graben. Their geometry therefore appears to be controlled by the graben structure that forms in the 305 center of the model above the crustal seed.

Interestingly, in brittle models with a initial phase of extension (e.g., model BI08, Figs. 4 and 11), not only the northern strike-slip faults orientation departs from the orientation expected from the Coulomb fracture criterion, but also the strike-slip faults that develop above the wedge in the southern part of the model. These faults with a larger than expected angle with respect to σ_1 also connect with the normal faults bounding the central graben formed during the initial phase of stretching. 310 These results highligth the fundamental role of pre-existing structures on the geometry of subsequent structures.

For models with a brittle-ductile crust, strike-slip faults are expected to range in between 30° and 45° following the Coulomb criterion and the slip-line theory (e.g., Anderson, 1905; Tapponnier and Molnar , 1976). Most of the strike-slip faults that cross-cut the models indeed show strikes compatible with the overall state of stress, i.e. N30-N45 for left-lateral strike-slip faults and

N135-N150 for right-lateral strike-slip faults. However, in models with an initial phase of stretching (e.g., model CE20, Figs. 9 and 11), strike-slip faults also develop with orientations almost parallel to the shortening direction. This clearly indicate that inherited structures, here in the form of previously developed N-S normal faults, control the subsequent location and geometry of structures.

Overall, our models show that whatever the strenght of the crust, its past deformation history and the relative ratio of extrusion rate over indentation rate, both normal faults and thrust faults remain with similar orientations, i.e. N-S and W-E, respectively. Instead, strike-slip faults exhibit a wide range of possible orientations with respect to the indentation (or extrusion) direction. As such they could give us insights into the tectonic context in which they formed. In particular wide angle conjugate strike-slip faults (with angles of up to ∼65° with respect to indentation direction) are found for strong crusts. They particularly form far away from the indentation location when the crust has not been previously deformed, but can also be observed closer from the indentation location if the crust has been previously extended. Instead, for weaker crusts, strike-slip faults can be parallel to the indentation direction in the case they reactivate former extensional structures.

4.3   Role of crustal strength in distribution of crustal deformation

Under comparable boundary conditions, the strength of the crust plays a fundamental role in controlling the location of deformation and the types of structures that accommodate deformation. Models without initial stretching phase and similar V_e/V_s (e.g., models BI09 and CE16, V_e/V_s = 0.9) exhibit significantly different patterns of deformation (Fig. 12). A strong crust (thick brittle part) favors the development of in-sequence E-W thrust faults verging to the north to accommodate indentation while extrusion is accommodated through N-S normal faults at the western and eastern boundaries of the model (Fig. 3). Instead, when the entire model is made of a weak crust, indentation results in a doubly-vergent system of conjugate E-W thrust faults and in large-scale conjugate strike-slip faults that also accommodate the extrusion. The lack of normal faults indicate that the horizontal stress remains high enough in the entire model to prevent the vertical stress to become σ_1. This can readily be explained by the decrease by a factor two of the thickness of the brittle crust in the "weak" models. Interestingly, in the strong model, there is also a variation in the thickness of the brittle part of the crust owing to the presence of the thin layer of silicone corresponding to the seed in the center of the model. However, it does not result in significant lateral variations in deformation style, due to the smaller variation in brittle thickness (decrease by 25%) and/or to the fact that the area of relatively weak crust only represents a small fraction of the entire model and that deformation is therefore controlled by the rest of the model. A more systematic change in the width and thickness of the weak part of the crust would be required to isolate the main controlling parameter.

Interestingly, model CE17, which shares the same boundary conditions as model CE16 but with an initial phase of W-E stretching exhibits a significantly different distribution of deformation during the second stage of deformation. This initial phase of stretching locally modifies the crustal strength by creating zones of thinned ductile and brittle portions of the crust accommodating the extension (Fig. 12). This has fundamental impact on the subsequent deformation pattern. Indeed, these areas of even weaker crust concentrate deformation through normal faulting or N-S strike-slip faulting that both were absent in model CE16. In turn, there are no thrust faults accommodating the indentation.

Experimental results again highlight the importance of past tectonic history and associated inherited structures and changes of crustal strength on the distribution of deformation and the types of structures that form during subsequent phases of de-

350 formation (Fig. 13). As such, the association of specific types of faults cannot be used as an indicator of the relative rate of indentation and extrusion unless previous history of deformation is properly constrained.

4.4 Basin reactivation under orthogonal contraction

Many modeling studies have previously investigated deformation associated with the inversion of extensional half-grabens subject to subsequent contraction (e.g., McClay , 1995; Bonini et al. , 2012; Zwaan et al. , 2022, and references therein). In

355 general, the applied directions of stretching and successive contraction are parallel (in 2D numerical or analog models) or oblique, but at low angles. Here, inspired by the San Jorge basin in Patagonia where some Cretaceous extensional structures were orthogonal to the Cenozoic contraction direction, we more specifically explored the conditions leading to reactivation of former extensional structures during successive orthogonal contraction (and parallel extension).

From our experimental dataset, there are no clear evidence that normal faults lying parallel to the contraction direction

360 are inverted as contractional structures during the second phase of deformation. While these areas are favorable to further contraction owing to their thinned crust and associated low vertical stress, the angular relationship between pre-existing normal faults and the direction of contraction ($\sim0°$) prevents the normal faults to be inverted. Instead, indentation is accommodated along contraction-orthogonal new thrust faults.

We further show that if extrusion orthogonal to the contraction direction is inhibited, there is no reactivation of preexisting

365 normal faults as normal faults or strike-slip faults (model BI01). Instead, allowing orthogonal extrusion always results in the reactivation of normal faults. However, different regimes are found depending on the boundary conditions and crustal strength. In models with low V_e/V_s and a weak crust (model CE18), extensional structures are preferentially reactivated as strike-slip faults, participating in the accommodation of the indentation that dominates. As V_e/V_s increases and becomes closer to 1, pre-existing normal faults are reactivated as either normal faults or strike-slip faults (models CE17 and CE20). Both types of faults

370 therefore develop and are juxtaposed as almost parallel structures without involving changes in boundary conditions. Finally, when extrusion rate dominates over indentation rate, pre-existing normal faults are reactivated as normal faults (models BI08 and BI11).

4.5 Application to natural cases and comparison with previous models

In our experiments, we did not intend to reproduce any specific natural case but rather systematically test internal and external

375 parameters. However, the analog models reproduce some of the deformation patterns documented in areas where deformation is accommodated by different combinations of normal, thrusts, and strike-slip faults. Hence, our experiments can be helpful to shed some light on the kinematics and rheological conditions behind these intricate geological settings.

In general, these complex structural frameworks take place during continental plate convergence, indentation, and subsequent lateral escape of lithospheric blocks during continental collisions (Tapponnier et al. , 1982) (Fig. 14). From our models,

380 we observe that at least two different deformation regimes coexist when V_e/V_s=0.7-0.9 and the three regimes operate simulta-

neously mostly when V_e/V_s is ≥ 1.4 (Figs. 3, 4, 5, 6, 7, 8, and 9). The latter could indicate a minimum value for this ratio for effective lateral escape to occur. In nature, the tectonic escape of crustal blocks takes place along conjugate strike-slip faults, commonly referred to as indent-linked strike-slip faults (Woodcock , 1986) or V-shaped conjugate strike-slip faults (e.g., Yin , 2010, and references therein) that take place along with variable degrees of crustal extension within the escaping crustal blocks.

385 Typical V-shaped conjugate faults have been documented in the Eastern Anatolia region (e.g., Şengör et al. , 1985; Dhont et al. , 2006; Hisarlı et al. , 2016, Fig. 14A), the eastern Alps (e.g., Ratschbacher et al. , 1991; Scharf et al. , 2013, Fig. 14B), the Tibetan plateau (e.g., Şengör and Kidd , 1979; Tapponnier et al. , 1982, Fig. 14C), and the central Asian intraplate region (e.g., Cunningham , 2005; Yin , 2010, Fig. 14D). Previous mantle-scale brittle-ductile analog experiments successfully reproduced the formation of V-shaped conjugate faults during continental indentation (e.g., Davy and Cobbold , 1988; Ratschbacher et al.

390 , 1991; Martinod et al. , 2000; Fournier et al. , 2004). However, a direct comparison with our models is difficult because these previous models were aimed at simulating larger domains (several hundreds kms) and the lateral escape of material was not kinematically controlled.

In our models, whether brittle or brittle-ductile, we also observe the development of conjugate strike-slips faults that are accompanied by different degrees of normal faulting during compression, which are reminiscent of those structural systems

395 seen in nature (BI05-08, Figs. 3 and 4; CE 16-20; Figs 6, 7, and 9). We nevertheless note that experiments including an overall weaker crust, simulated by adding a silicon layer as an analog for ductile lower crust materials, are more prone to have well-developed conjugate strike-slip systems that cross-cut the entire model (CE 16-20; Figs 6, 7, and 9). Our results are partly similar to those by Dhifaoui et al. (2021) (model M-3), in which crustal-scale brittle-ductile analog models were subjected to simultaneous shortening and orthogonal extension imposed by one piston in each direction. Despite the slightly different

400 boundary conditions (stretching being allowed only along one boundary), both approaches show crustal escape through a V-shaped strike-slips system. This is compatible with natural examples analyzed in Fig. 14A,B,C,D, where Cenozoic conjugate strike-slip systems formed onboard thick and hot, and hence, weak orogenic crusts of the Anatolian and Tibetan plateaus, Central Asian intraplate orogenic system, and the Alpine orogen. Therefore, a weak crust is an important factor contributing to lateral tectonic escape in those settings by allowing the formation of fault-bounded brittle upper crust blocks translated laterally

405 by strike-slip systems and constrictional ductile flow in the lower crust (Ratschbacher et al. , 1991; Scharf et al. , 2013).

In models that include an initial phase of extension, and under the applied boundary conditions, we observe variable degrees of extensional to strike-slip reactivation of the previous extensional basins during basin-parallel shortening (BI08-11 and CE 17-20, Figs. 4, 7, and 8). These results differ from previous basin inversion analog models by Del Ventisette et al. (2006); Sani et al. (2007); Deng et al. (2020), which also applied a basin-parallel shortening after a first stage of orthogonal extension. In

410 these models, despite the high obliquity angle between basin strike and shortening direction, thrust faults formed parallel or at a low angle with the shortening direction, ultimately producing basin inversion. A difference in boundary conditions applied in our models BI08-11 and CE 17-20, where active orthogonal extension took place during shortening, could explain why basin inversion does not occur in our models. However, model BI01, shared similar boundary conditions with previous studies with no extension applied during shortening and it does not show any evidence of shortening-parallel thrusting during the second stage

415 of deformation (Fig. 4). This implies that not only boundary conditions but also internal parameters are crucial in allowing basin

inversion during orthogonal shortening. The presence of a larger seed to localize the initial extension, a thinner rift basin crust, and inclusion of synrift sediments, may yield a comparably weaker crustal area leading to an easier localization of deformation during compression. Besides these contrasting results, our models are compatible with natural cases of synorogenic foreland rifting-transtensional reactivations that are complex processes of basin reactivation during regional compression (Gianni et al.

420 , 2015). These cases have been well documented in the Baikal region in Central Asia (Mats and Perepelova , 2011; Mats , 2013) (Mats and Perelepova, 2011; Mats, 2013) and some places in South America such as in Central Patagonia (Gianni et al. , 2015) (Figs. 14E and D). In both cases, former extensional basins disposed orthogonal to neighboring plate margins, where subsequently reactivated by a distal basin-parallel compressional stress field (Figs. 14E and D).

5   Conclusions

425 Analog experiments involving simultaneous shortening and orthogonal extension under different boundary and rheological conditions, and including the effect of crustal inheritance on fault reactivation allow us to gain new insights into geological areas recording the simultaneous activity of different deformation regimes. Our experiments corroborate that crustal deformation takes place through a combination of normal faults, thrust faults, and strike-slip faults when boundary conditions satisfy non plane-strain conditions. In this case, the type of structures and their location depend on the applied boundary conditions and

430 the inclusion of pre-existing heterogeneities.

For brittle models, the coexistence of the three types of structures is possible for intermediate ratios of extrusion rate over indentation rate ($1.4 < V_e/V_s < 2$). For lower V_e/V_s, the larger principal stress (σ_1) remains horizontal and parallel to the shortening direction, excepted at the edges of the model where it becomes vertical producing shortening-parallel normal faults. For values of $V_e/V_s \geq 2$, shortening-parallel horizontal stress is not high enough to become the maximum stress axis, thus

435 inhibiting failure of the crust along shortening-orthogonal thrust faults. For brittle-ductile models, we do not observe the coexistence of the three types of structures. We observe either shortening-orthogonal thrust faults associated with conjugate strike-slip faults (model with low V_e/V_s and no initial extensional phase) or shortening-parallel normal faults associated with conjugate strike-slip faults (model with high V_e/V_s and initial extensional phase).

Our models also show that whatever the crustal strength, its past deformation history, and V_e/V_s ratio, both normal and

440 thrust faults remain with similar orientations, i.e. shortening-parallel and shortening-orthogonal, respectively. Instead, strike-slip faults exhibit a wide range of possible orientations with respect to the shortening (or extension) direction. In particular, wide angle conjugate strike-slip faults with angles of up to ~65° with respect to shortening direction occur when deforming a strong crust. These faults develop far from the indentation location when the crust has not been previously deformed or closer from the indentation location if the crust has been previously extended. Instead, for weaker crusts, strike-slip faults

445 can be parallel to the indentation direction in the case they reactivate former extensional structures. Furthermore, we note that under comparable boundary conditions, the strength of the crust plays a fundamental role in controlling the location of deformation and the types of structures that accommodate deformation, highlighting the importance of inherited structures and

changes of crustal strength on the distribution of deformation and the types of structures that form during subsequent phases of deformation.

450   Finally, our models reproduce some of the deformation patterns documented in natural cases where deformation took place through a complex combination of normal, thrusts, and strike-slip faults. From these experiments, we observe that at least two different deformation regimes coexist when the V_e/V_s is ≥ 0.9 and the three regimes operate simultaneously when V_e/V_s is ≥ 1.4, possibly indicating a minimum value in this ratio for effective lateral scape to take place. Independently of the crustal rheology or the presence of crustal weaknesses, we observe the development of conjugate strike-slips faults accompanied

455   by variable normal faulting during compression/indentation. This is reminiscent of those structural systems seen in nature accommodating tectonic escape of crustal blocks in Central Asia, eastern Alps, eastern Anatolia, and the Tibetan plateau. Our results indicate that the conjugate strike-slip systems are favored by an overall weaker crust, which is consistent with observations in the former orogenic areas. In models that include an initial phase of extension, we observe variable degrees of extensional to strike-slip reactivation of the previous extensional basins during basin-parallel shortening that are compatible

460   with Late Mesozoic examples in the San Jorge basin in Patagonia and the Baikal rift.

Data availability. Time-series of top-view pictures and strain analysis in the form of movies for the 12 experiments are available through the GFZ Data Services (Guillaume et al. , 2022):

https://dataservices.gfz-potsdam.de/panmetaworks/review/7350e22e83d36b8f48363bc1d4266552e98f7f5e9059bda09471907a1988507d/

Author contributions. B. Guillaume helped in the design of the experiments, participated in running the models, conducted the analysis of

465   the experiments and co-wrote the manuscript. G. Gianni ran some of the experiments and co-wrote the manuscript. J.J.- Kermarrec designed the experiments and K. Bock conducted some of the experiments.

Competing interests. The authors declare no competing interests.

Acknowledgements. G.M.G acknowledges the support given by CONICET.

References

470   Anderson, E.M.: The Dynamics of Faulting, Transactions of the Edinburgh Geological Society, 8, 387-402, 1905.

Barnes, J. B. and Ehlers, T. A.: End member models for Andean Plateau uplift, Earth-Sci. Rev., 97(1-4), 105-132, 2009.

Berglar, K., Gaedicke, C., Franke, D., Ladage, S., Klingelhoefer, F., and Djajadihardja, Y. S.: Structural evolution and strike-slip tectonics off north-western Sumatra. Tectonophysics, 480(1-4), 119-132, 2010.

Bonini, M., Sani, F., and Antonielli, B.: Basin inversion and contractional reactivation of inherited normal faults: A review based on previous
475   and new experimental models, Tectonophysics, 522, 55-88, 2012.

Broerse, T., Krstekanić, N., Kasbergen, C., and Willingshofer, E.: Mapping and classifying large deformation from digital imagery: application to analogue models of lithosphere deformation, Geophysical Journal International, 226(2), 984-1017, 2021.

Brun, J.-P.: Narrow rifts versus wide rifts: inferences for the mechanics of rifting from laboratory experiments, Philos. Trans. Royal Soc., 357, 695–712, 1999.

480   Buck, W. R.: Models of Continental Lithospheric Extension, J. Geophys. Res., 96, 20,161- 1201 20,178, https://doi.org/10.1029/91JB01485, 1991.

Buiter, S. J., and Adrian Pfiffner, O.: Numerical models of the inversion of half-graben basins. Tectonics, 22(5), 2003.

Burbidge, D. R., and Braun, J.: Numerical models of the evolution of accretionary wedges and fold-and-thrust belts using the distinct-element method. Geoph. J. Int., 148(3), 542-561, 2002.

485   Bürgman, R., and Dresen, G.: Rheology of the Lower Crust and Upper Mantle: Evidence from Rock Mechanics, Geodesy, and Field Observations, Annu. Rev. Earth Pl. Sc., 36, 531-67, 1209 https://doi.org/10.1146/annurev.earth.36.031207.124326, 2008.

Byerlee, J. (1978). Friction of rocks. In Rock friction and earthquake prediction (pp. 615-626). Birkhäuser, Basel.

Cembrano, J., Hervé, F., and Lavenu, A.: The Liquiñe Ofqui fault zone: a long-lived intra-arc fault system in southern Chile, Tectonophysics, 259(1-3), 55-66, 1996.

490   Chemenda, A., Lallemand, S., and Bokun, A.: Strain partitioning and interplate friction in oblique subduction zones: Constraints provided by experimental modelling, J. Geoph. Res.: Solid Earth, 105(B3), 5567-5581, 2000.

Chorowicz, J.: The east African rift system. J. African Earth Sci., 43(1-3), 379-410, 2005.

Cunningham, D.: Active intracontinental transpressional mountain building in the Mongolian Altai: defining a new class of orogen, Earth Planet. Sci. Lett. , 240(2), 436-444, 2005.

495   Davis, D., Suppe, J., and Dahlen, F. A.: Mechanics of fold-and-thrust belts and accretionary wedges, J. Geophys. Res: Solid Earth, 88(B2), 1153-1172, 1983.

Davy, P., and Cobbold, P. R.: Indentation tectonics in nature and experiment. 1. Experiments scaled for gravity. Bull. Geol. Inst. Univ. Uppsala, 14, 129-141, 1988.

Del Ventisette, C., Montanari, D., Sani, F., and Bonini, M.: Basin inversion and fault reactivation in laboratory experiments, J. Struct.
500   Geol., 28(11), 2067-2083, 2006.

Deng, H., Koyi, H. A., and Zhang, J.: Modelling oblique inversion of pre-existing grabens. Geol. Soc. Lon. Spec. Pub., 487(1), 263-290, 2020.

Dèzes, P., Schmid, S. M., and Ziegler, P. A.: Evolution of the European Cenozoic Rift System: interaction of the Alpine and Pyrenean orogens with their foreland lithosphere., Tectonophysics, 389(1-2), 1-33, 2004.

505 Dhifaoui, R., Strzerzynski, P., Mourgues, R., Rigane, A., Gourmelen, C., and Peigné, D.: Accommodation of compression and lateral exten-
sion in a continental crust: Analogical modeling of the Central Atlas (eastern Algeria, Tunisia) and Pelagian sea, Tectonophysics, 817,
229052, 2021.

Dhont, D., Chorowicz, J., Luxey, P.: Anatolian escape tectonics driven by Eocene crustal thickening and Neogene–Quaternary extensional
collapse in the eastern Mediterranean region, in: Postcollisional tectonics and magmatism in the Mediterranean region and Asia, edited by

510 Dilet, Y., Pavilides, S., Geol. Soc. Spec. Pap., 409, pp. 331–462, 2006.

Dooley, T. P., and Schreurs, G.: Analogue modelling of intraplate strike-slip tectonics: A review and new experimental results, Tectono-
physics, 574, 1-71, 2012.

Dickinson, W. R.: The Basin and Range Province as a composite extensional domain. Int. Geol. Rev., 44(1), 1-38, 2002.

Fournier, M., Jolivet, L., Davy, P., and Thomas, J. C.: Backarc extension and collision: an experimental approach to the tectonics of Asia,

515 Geoph. J. Int., 157(2), 871-889, 2004.

Giambiagi, L., Alvarez, P., and Spagnotto, S.: Temporal variation of the stress field during the construction of the central Andes: Constrains
from the volcanic arc region (22–26°S), Western Cordillera, Chile, during the last 20 Ma, Tectonics, 35(9), 2014-2033, 2016.

Gianni, G. M., Navarrete, C. G., and Folguera, A.: Synorogenic foreland rifts and transtensional basins: A review of Andean imprints on the
evolution of the San Jorge Gulf, Salta Group and Taubaté Basins. J. S. Am. Earth Sci., 64, 288-306, 2015.

520 Graveleau, F., Malavieille, J., and Dominguez, S. (2012). Experimental modelling of orogenic wedges: A review. Tectonophysics, 538, 1-66.

Guillaume, B., Funiciello, F., and Faccenna, C.: Interplays Between Mantle Flow and Slab Pull at Subduction Zones in 3D, J. Geoph. Res.,
126(5), e2020JB021574, 2021.

Guillaume, B., Gianni, G. Kermarrec, J.-J., and Bock, K.: Experimental data of analogue models addressing the influence of crustal
strength, tectonic inheritance and extrusion/indentation rates on crustal deformation and basin reactivation. GFZ Data Services, 2022.

525 https://doi.org/10.5880/fodgeo.2022.011

Handin, J., (1969). On the Coulomb–Mohr failure criterion. J. Geoph. Res., 74, 5343–5348.

Harland, W. B., and Bayly, M. B.: Tectonic regimes. Geol. Mag., 95(2), 89-104, 1958.

Hilde, T. W., Uyeda, S., and Kroenke, L.: Evolution of the western Pacific and its margin, Tectonophysics, 38(1-2), 145-165, 1977.

Hisarlı, Z. M., Çinku, M. C., Ustaömer, T., Keskin, M., and Orbay, N. Neotectonic deformation in the Eurasia–Arabia collision zone, the

530 East Anatolian Plateau, E Turkey: evidence from palaeomagnetic study of Neogene–Quaternary volcanic rocks. International Journal of
Earth Sciences, 105(1), 139-165, 2016.

Hubbert, M. K.: Theory of scaled models as applied to the study of geological structures, Geol. Soc. Am. Bull., 48, 1459-1520, 1937.

Jaeger, J.C., and Cook, N.G.W.,: Fundamentals of Rock Mechanics. Chapman and Hall, Wiley, New York, 585 pp, 1976.

Klinkmüller, M., Schreurs, G., Rosenau, M., and Kemnitz, H.: Properties of granular analogue model materials: A community wide survey,

535 Tectonophysics, 684, 23-38, 2016.

Koyi, H.: Mode of internal deformation in sand wedges. J. Struct. Geol., 17(2), 293-300, 1995.

Lohrmann, J., Kukowski, N., Adam, J., and Oncken, O.: The impact of analogue material properties on the geometry, kinematics, and
dynamics of convergent sand wedges, J. Struct. Geol., 25(10), 1691-1711, 2003.

Lu, H., Tian, X., Yun, K., and Li, H.: Convective removal of the Tibetan Plateau mantle lithosphere by ∼26 Ma, Tectonophysics, 731, 17-34,

540 2018.

Martinod, J., Hatzfeld, D., Davy, P., Gautier, P. and Brun, J.P.: Continental collision, gravity spreading, and kinematics of Aegea and Anatolia,
Tectonics, 19 (2), 290-299, 2000.

Mats, V.D. and Perepelova, T.I.: A new perspective on evolution of the Baikal Rift, Geosci. Front. 2, 349-365, 2011.

Mats, V.D.: Late cretaceous and cenozoic stratigraphy of the Baikal Rift sediments, Stratigr. Geol. Correl. 21, 637-651, 2013.

545 McClay, K.R.: The geometries and kinematics of inverted faults systems: a review of analogue modelling studies, Geol. Soc. Spec. Publ., 88, 97-118, 1995.

McClay, K. and Bonora, M.: Analog models of restraining stepovers in strike-slip fault systems, AAPG bulletin, 85(2), 233-260, 2001.

Molnar, P. and Tapponnier, P.: Active tectonics of Tibet. J. Geoph. Res.: Solid Earth, 83(B11), 5361-5375, 1978.

Molnar, P. and Dayem, K. E.: Major intracontinental strike-slip faults and contrasts in lithospheric strength, Geosphere, 6(4), 444-467, 2010.

550 Mouthereau, F., Filleaudeau, P.-Y., Vacherat, A., Pik, R., Lacombe, O., Fellin, M.G., Castelltort, S., Christophoul, F., and Masini, E.: Placing limits to shortening evolution in the Pyrenees: Role of margin architecture and implications for the Iberia/Europe convergence, Tectonics, 33, 2283-2314, 2014.

Mugnier, J. L., Baby, P., Colletta, B., Vinour, P., Bale, P., and Leturmy, P.: Thrust geometry controlled by erosion and sedimentation: A view from analogue models, Geology, 25(5), 427-430, 1997.

555 Munteanu, I., Willingshofer, E., Sokoutis, D., Matenco, L., Dinu, C., and Cloetingh, S.: Transfer of deformation in back-arc basins with a laterally variable rheology: Constraints from analogue modelling of the Balkanides–Western Black Sea inversion, Tectonophysics, 602, 223-236, 2013.

Oncken O., Hindle D., Kley J., Elger K., Victor P., and Schemmann K.: Deformation of the Central Andean Upper Plate System - Facts, Fiction, and Constraints for Plateau Models, in: The Andes, edited by Oncken O. et al. Springer, Berlin, Heidelberg, 2006.

560 Pfiffner, O. A.: Thick-skinned and thin-skinned tectonics: a global perspective, Geosciences, 7(3), 71, 2017.

Pinto, L., Muñoz, C., Nalpas, T., and Charrier, R.: Role of sedimentation during basin inversion in analogue modelling, J. Struct. Geol., 32(4), 554-565, 2010.

Raleigh, C.B., and Paterson, M.S.: Experimental deformation of serpentinite and its tectonic implications, J. Geoph. Res.: Solid Earth, 70, 3965-3985, 1965.

565 Ramberg, H.: Gravity, Deformation and the Earth's Crust, Academic Press, London, 1981.

Ratschbacher, L., Merle, O., Davy, P., and Cobbold, P.: Lateral extrusion in the Eastern Alps, part 1: boundary conditions and experiments scaled for gravity, Tectonics, 10(2), 245-256, 1991.

Royden, L. H., Burchfiel, B. C., and van der Hilst, R. D.: The geological evolution of the Tibetan Plateau, Science, 321(5892), 1054-1058, 2008.

570 Rudolf, M., Boutelier, D., Roseneau, M., Schreurs, G., and Oncken, O.: Rheological benchmark of silicone oils used for analog modeling of short- and long-term lithospheric deformation, Tectonophysics, 684, 12-22, 2016.

Saint-Carlier, D., Charreau, J., Lavé, J., Blard, P. H., Dominguez, S., Avouac, J. P., and ASTER Team.: Major temporal variations in shortening rate absorbed along a large active fold of the southeastern Tianshan piedmont (China). Earth Planet. Sci. Lett., 434, 333-348, 2016.

Sani, F., Del Ventisette, C., Montanari, D., Bendkik, A., and Chenakeb, M.: Structural evolution of the Rides Prerifaines (Morocco): structural
575 and seismic interpretation and analogue modelling experiments. Int. J. Earth Sci., 96(4), 685-706, 2007.

Saria, E., Calais, E., Stamps, D.S. Delvaux, D., and Hartnady, C.J.H.: Present-day kinematics of the East African Rift, J. Geophys. Res.: Solid Earth, 119, 3584-3600, 2014.

Scharf, A., Handy, M. R., Favaro, S., Schmid, S. M., and Bertrand, A.: Modes of orogen-parallel stretching and extensional exhumation in response to microplate indentation and roll-back subduction (Tauern Window, Eastern Alps). Int. J. Earth Sci., 102(6), 1627-1654, 2013.

580 Sengör, A. M. C.: Collision of irregular continental margins: Implications for foreland deformation of Alpine-type orogens, Geology, 4(12), 779-782, 1976.

Şengör, A.M.C., Kidd, W.S.F.: Post-collisional tectonics of the Turkish–Iranian plateau and a comparison with Tibet, Tectonophysics, 55, 361–376, 1979.

Şengör, A. M. C., Görür, N., Şaroğlu, F.: Strike-Slip Faulting and Related Basin Formation in Zones of Tectonic Escape: Turkey as a
585 Case Study, in: Strike-Slip Deformation, Basin Formation, and Sedimentation, edited by Biddle, K.T., Christie-Blick, N., SEPM Special Publication, 37, 1985.

Simpson, G.: Mechanics of non-critical fold–thrust belts based on finite element models, Tectonophysics, 499(1-4), 142-155, 2011.

Sternai, P., Jolivet, L., Menant, A., and Gerya, T.: Driving the upper plate surface deformation by slab rollback and mantle flow, Earth Planet. Sci. Lett., 405, 110-118, 2014.

590 Sternai, P., Sue, C., Husson, L., Serpelloni, E., Becker, T. W., Willett, S. D., et al.,: Present-day uplift of the European Alps: Evaluating mechanisms and models of their relative contributions, Earth-Sci. Rev., 190, 589-604, 2019.

Sutherland, R., Davey, F., and Beavan, J.: Plate boundary deformation in South Island, New Zealand, is related to inherited lithospheric structure, Earth Planet. Sci. Lett., 177(3-4), 141-151, 2000.

Takagi, H.: Implications of mylonitic microstructures for the geotectonic evolution of the Median Tectonic Line, central Japan. J. Struct.
595 Geol., 8(1), 3-14, 1986.

Tapponnier, P., and Molnar, P.: Slip-line field theory and large-scale continental tectonics, Nature, 264, 319-324.

Tapponnier, P., Peltzer, G. L. D. A. Y., Le Dain, A. Y., Armijo, R., and Cobbold, P.: Propagating extrusion tectonics in Asia: New insights from simple experiments with plasticine, Geology, 10(12), 611-616, 1982.

Tapponnier, P., Zhiqin, X., Roger, F., Meyer, B., Arnaud, N., Wittlinger, G., and Jingsui, Y.: Oblique stepwise rise and growth of the Tibet
600 Plateau, science, 294(5547), 1671-1677, 2001.

Tatar, M., Hatzfeld, D., Martinod, J., Walpersdorf, A., Ghafori-Ashtiany, M., and Chéry, J.: The present-day deformation of the central Zagros from GPS measurements, Geoph. Res. let., 29(19), 33-1, 2002.

Thielicke, W. and Sonntag, R.: Particle Image Velocimetry for MATLAB: Accuracy and Enhanced Algorithms in PIVlab, J. Open Res. Softw., 2021.

605 Twiss, R.J. and Moores, E.M.: Structural Geology. W.H. Freeman and Company, New York, 532, 1992.

Vendeville, B., Cobbold, P. R., Davy, P., Brun, J. -P., and Choukroune, P.: Physical models of extensional tectonics at various scales, in: Continental Extensional Tectonics, edited by: 31 1Coward, M. P., Dewey, J. F., and Hancock, P. L., Geol Soc. Spec. Publ., 28, 95-107, 1987.

Weijermars, R., and Schmeling, H.: Scaling of Newtonian and non-Newtonian fluid dynamics 1578 without inertia for quantitative modelling
610 of rock flow due to gravity (including the concept of rheological similarity), Phys. Earth Planet. In., 43, 316-330, 1986.

Woodcock, N. H.: The role of strike-slip fault systems at plate boundaries. Phil.Trans.R.Soc., 317(1539), 13-29, 1986.

Yin, A.: Cenozoic tectonic evolution of Asia: A preliminary synthesis, Tectonophysics, 488(1-4), 293-325, 2010.

Zoback, M. L.: First-and second-order patterns of stress in the lithosphere: The World Stress Map Project. J. Geoph. Res.: Solid Earth, 97(B8), 11703-11728, 1992.

615 Zwaan, F., Schreurs, G., Naliboff, J., and Buiter, S.J.H.: Insights into the effects of oblique extension on continental rift interaction from 3D analogue and numerical models, Tectonophysics, 693, 239-260, https://doi.org/10.1016/j.tecto.2016.02.036, 2016.

Zwaan, F., Schreurs, G., and Buiter, S. J. H.: A systematic comparison of experimental set-ups for modelling extensional tectonics, Solid Earth, 10, 1063–1097, 2019.

Zwaan, F., Chenin, P., Erratt, D., Manatschal, G., and Schreurs, G.: Complex rift patterns, a result of interacting crustal and mantle weaknesses, or multiphase rifting? Insights from analogue models, Solid Earth, 12, 1473-1495, 2021.

Zwaan, F., Schreurs, G., Buiter, S., Ferrer, O., Reitano, R., Rudolf, M., and Willingshofer, E.: Analogue modelling of basin inversion: a review and future perspectives, Solid Earth Discuss. [preprint], https://doi.org/10.5194/se-2022-8, in review, 2022.

620
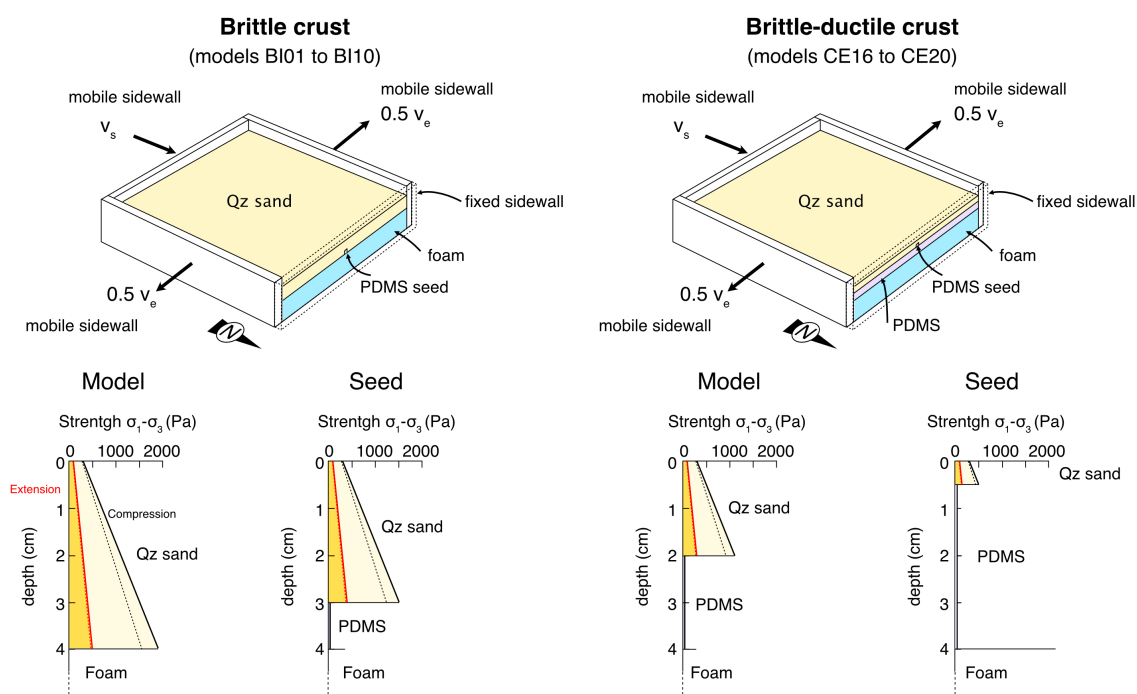
Figure 1. Experimental set-up (top) and corresponding strength enveloppes (bottom) under extension and compression for the two types of models with brittle crust ("strong" crust) and a brittle-ductile crust ("weak" crust). Solid lines corresponds to the peak friction for Qz sand and dashed lines to the reactivation friction.
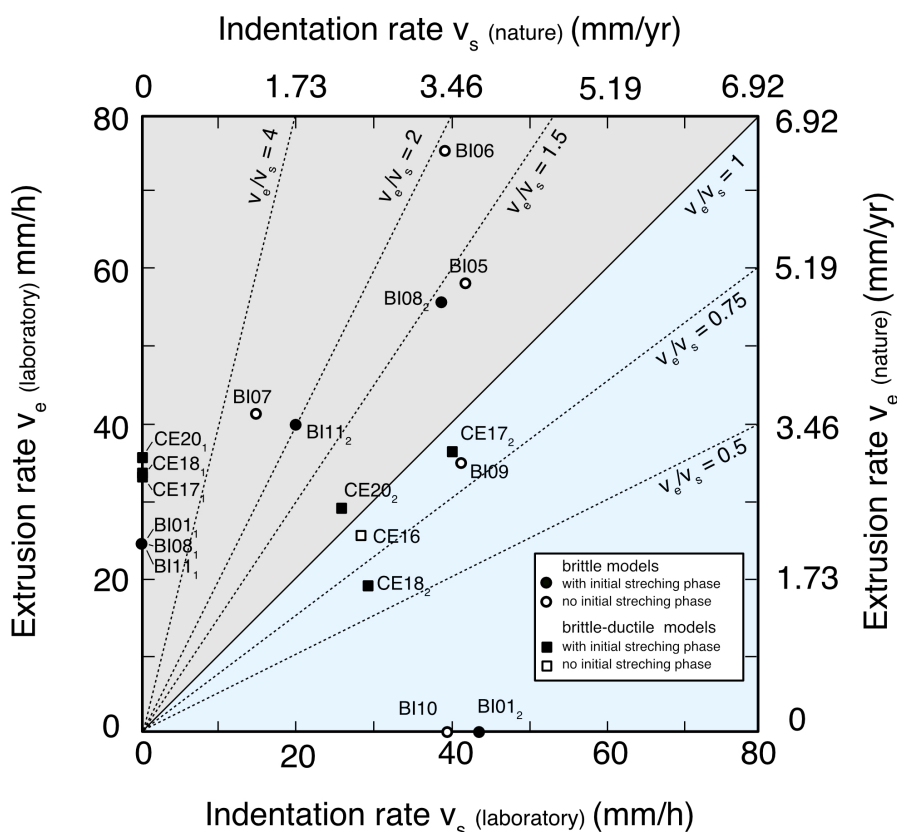
Figure 2. Applied boundary kinematic conditions for models with brittle crust (circles) and brittle-ductile crust (squares). Models with two stages of deformation have black filled symbols and subscripts to indicate the stage of deformation. Laboratory and scaled values are given for the shortening (indentation) and stretching (extrusion) rates.
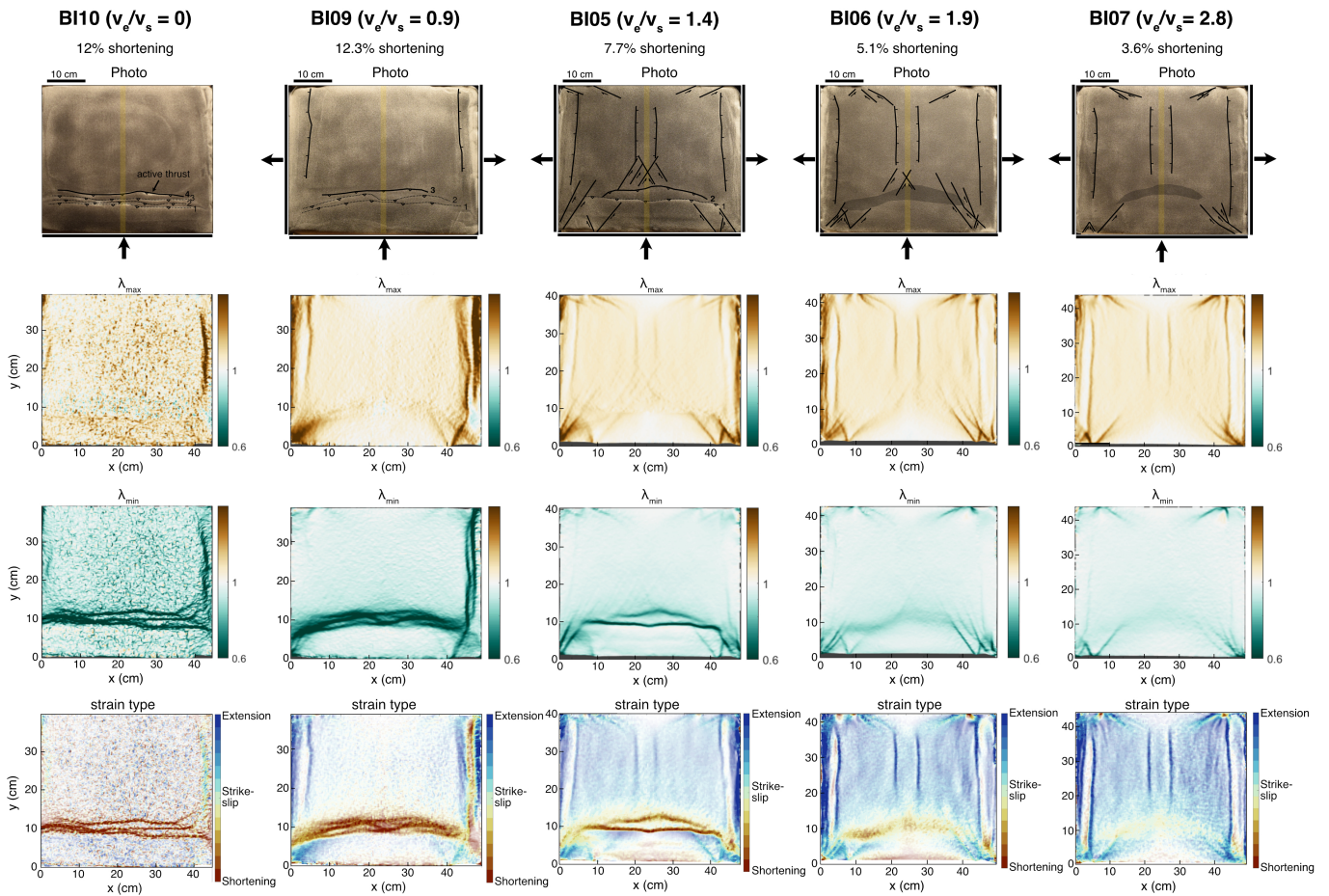
Figure 3. Interpreted pictures, principal stretches λ_{max}, λ_{min} ($\lambda = 1$ represents no length change) and strain type after 10% of along-x stretching for brittle models BI10, BI09, BI05, BI06, and BI07: shortening (red), strike-slip (green) and stretching (blue), with intermediate, oblique deformation at intermediate colors. The corresponding amount of shortening is indicated at the top. For model BI10, there is no along-x stretching and deformation is shown after 12% of along-y shortening (almost similar to model BI09).
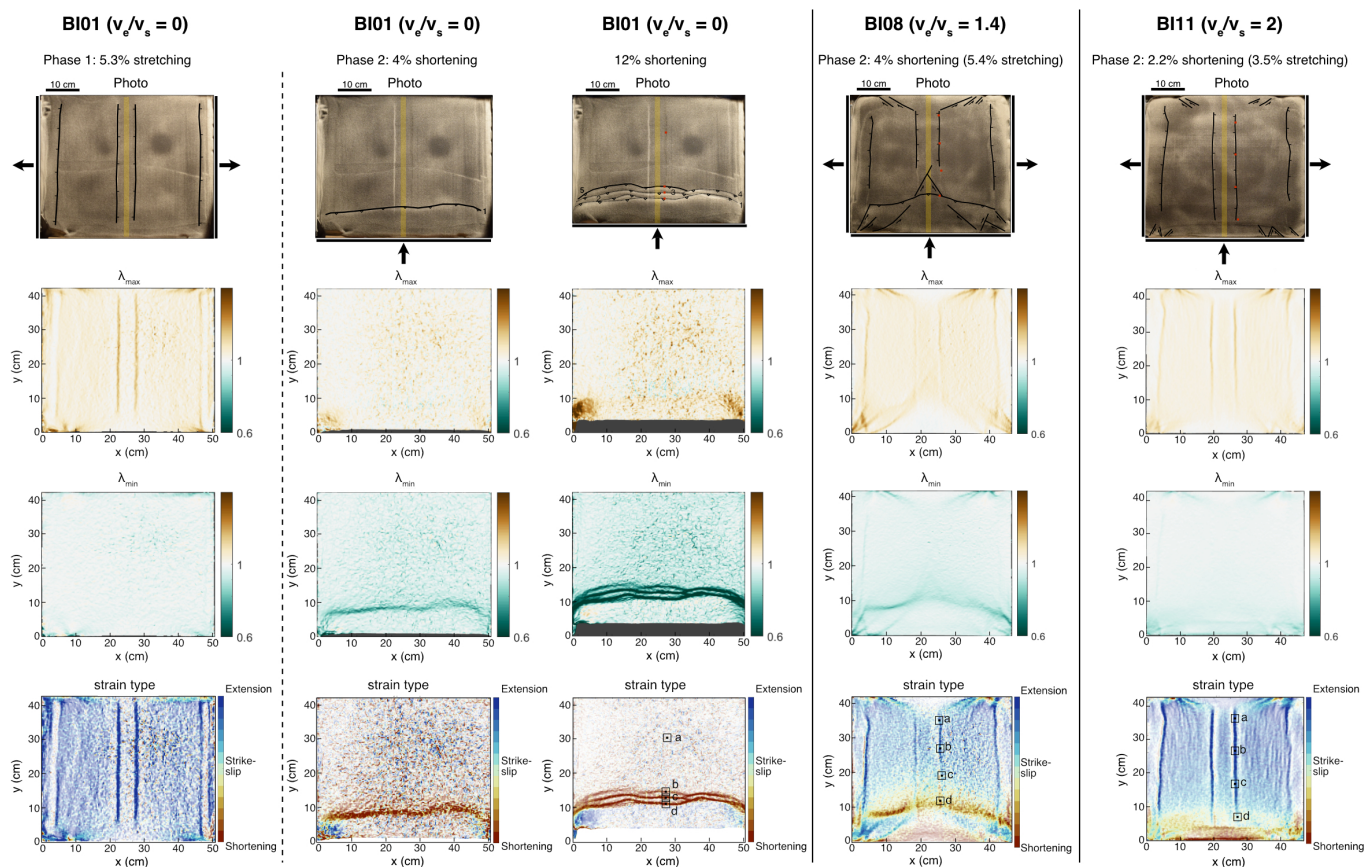
Figure 4. Interpreted pictures, principal stretches λ_{max}, λ_{min} ($\lambda = 1$ represents no length change) and strain type for brittle models BI01, BI08 and BI11: shortening (red), strike-slip (green) and stretching (blue), with intermediate, oblique deformation at intermediate colors. The amount of imposed stretching during the first stage is ~5% for the 3 models. The amount of shortening and stretching during the second stage is indicated at the top.
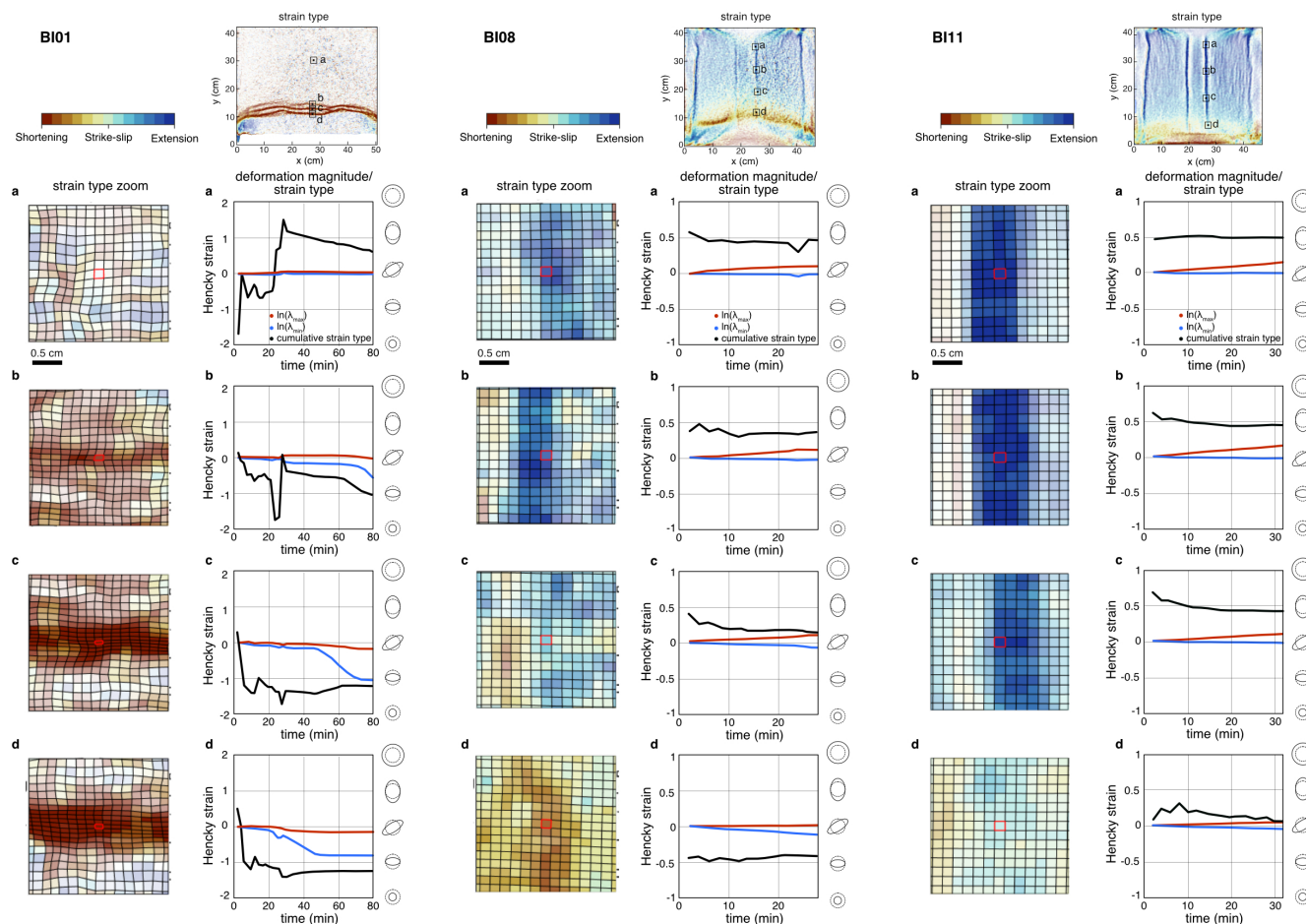
Figure 5. Temporal evolution of principal stretches and strain type during the second stage of deformation for points a, b, c and d in models BI01, BI08, and BI11 (brittle-only crust). Upper right-hand panel: strain type (final) and overview of the selected areas. Left column: zoom on the strain type and the selected grid cell (which is outlined in red, neighbouring cells outlined in black). Right column: time-evolution of the logarithm of the two principal stretches (Hencky strain; blue and red curves) and associated strain type (cumulative; black curve, right axis).

Figure 6. Interpreted pictures, principal stretches λ_{max}, λ_{min} ($\lambda = 1$ represents no length change) and strain type for model CE16 after 4% of shortening, 5 and 10% of stretching: shortening (red), strike-slip (green) and stretching (blue), with intermediate, oblique deformation at intermediate colors.
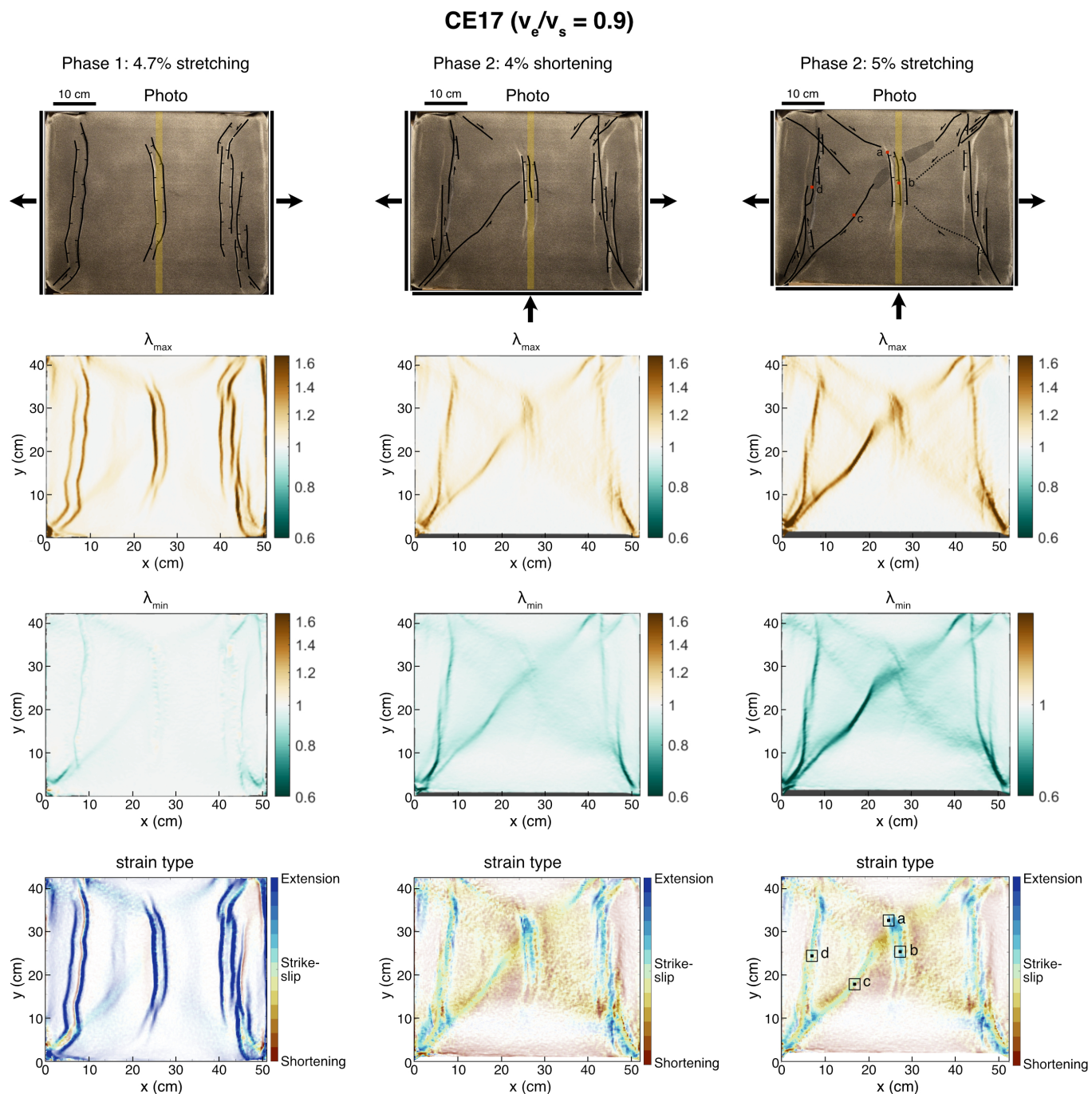
Figure 7. Interpreted pictures, principal stretches λ_{max}, λ_{min} ($\lambda = 1$ represents no length change) and strain type for model CE17 after a first phase of E-W 4.7% stretching, 4% of shortening, and 5% of stretching: shortening (red), strike-slip (green) and stretching (blue), with intermediate, oblique deformation at intermediate colors.
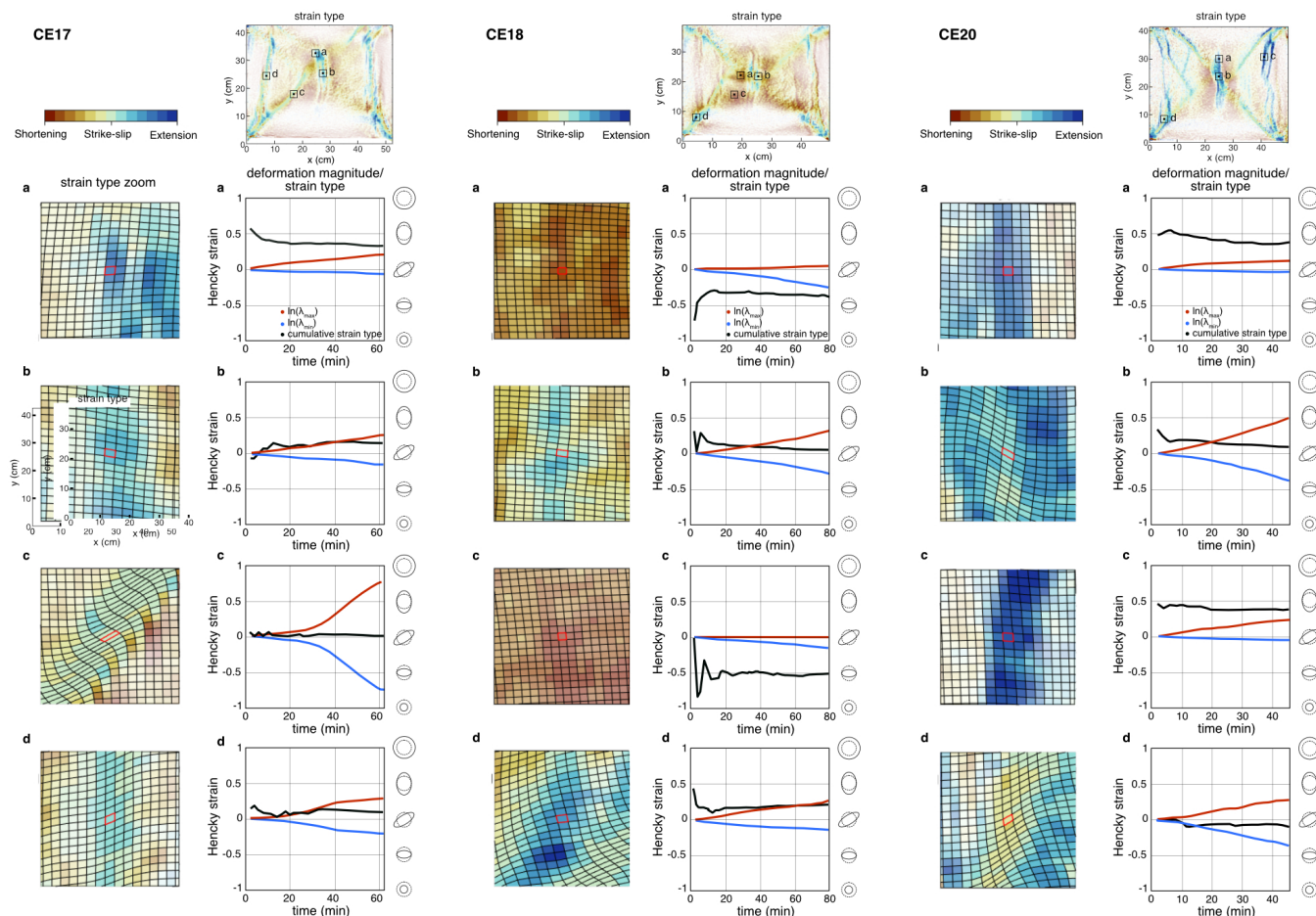
Figure 8. Temporal evolution of principal stretches and strain type during the second stage of deformation for points a, b, c and d in models CE17, CE18, and CE20 (brittle-ductile crust). Upper right-hand panel: strain type (final) and overview of the selected areas. Left column: zoom on the strain type and the selected grid cell (which is outlined in red, neighboring cells outlined in black). Right column: time-evolution of the logarithm of the two principal stretches (Hencky strain; blue and red curves) and associated strain type (cumulative; black curve, right axis).
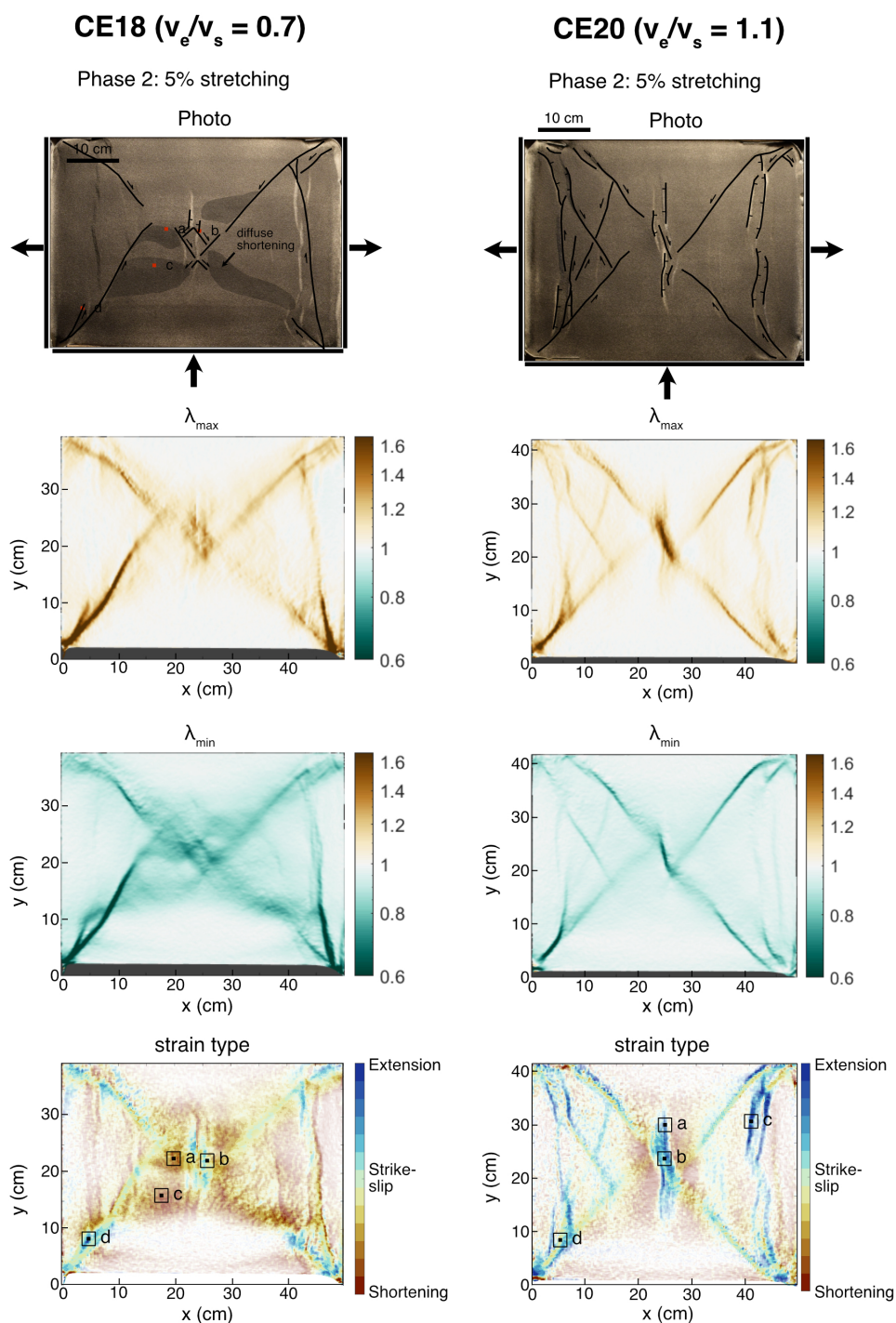
Figure 9. Interpreted pictures, principal stretches λ_{max}, λ_{min} ($\lambda = 1$ represents no length change) and strain type for models CE18 and CE20 after 5% of stretching: shortening (red), strike- slip (green) and stretching (blue), with intermediate, oblique deformation at intermediate colors.
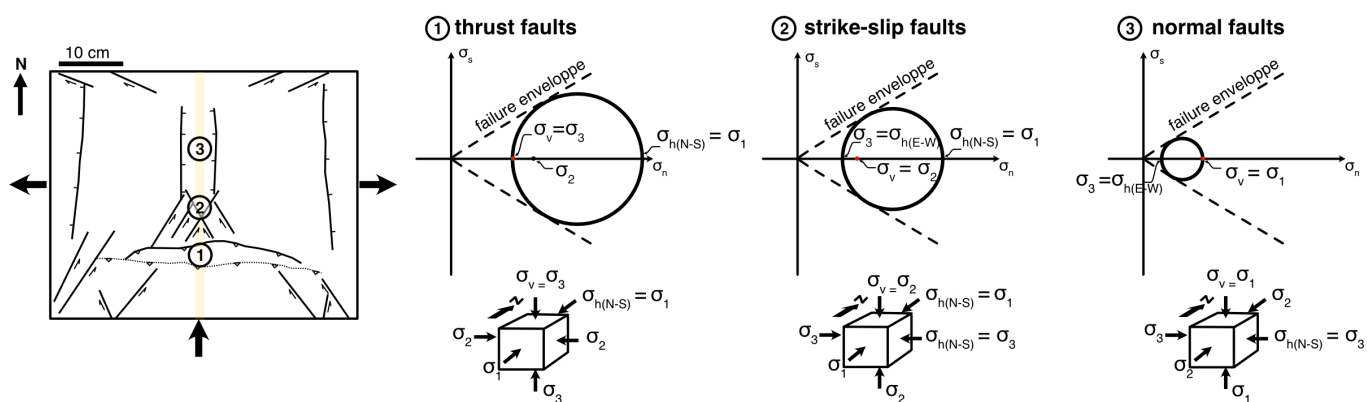
Figure 10. Interpreted distribution of structures for model BI05 after 7.7% of shortening, and corresponding principal stress axis and Mohr-Coulomb analysis for the areas with labels 1, 2 and 3 on the left figure.
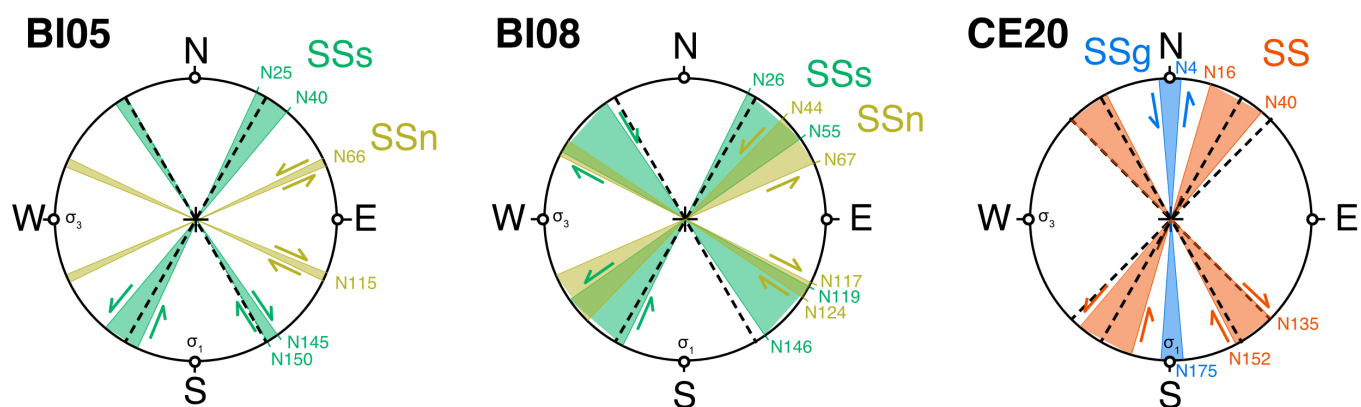
Figure 11. Stereoplots showing the ranges of orientations and the relative motion of strike-slip faults located in the northern (SSn) and southern (SSs) parts of models BI05 (left) and BI08 (right), after a total of around 10% of E-W stretching (see Figs. 3 and 4) as well as in the underformed (SS) and previously deformed (SSg) parts of model CE20 (right) after 5% of stretching (see Fig. 9). The black dotted lines indicate angles of 30° and 45° with respect to a N-S σ_1.
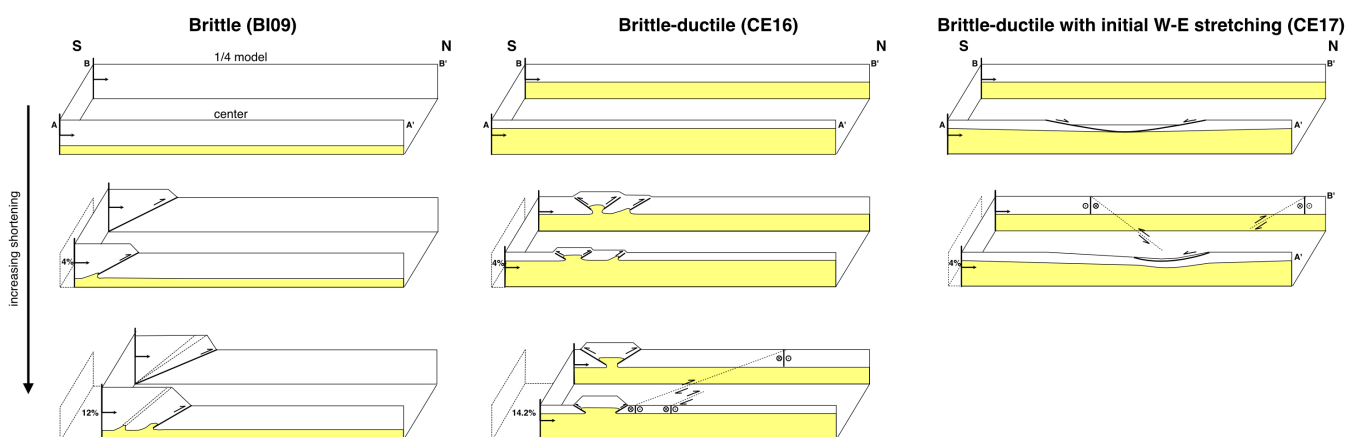
Figure 12. N-S cross-sections interpreted from top pictures before deformation (top row), after 4% of shortening (central row) and after 12 to 14% of shortening (bottom row) for models with comparable ratios of extrusion over indentation rates V_e/V_s = 0.9. For each model, section AA' corresponds to the center of the model and B-B' to the western quarter of the model.
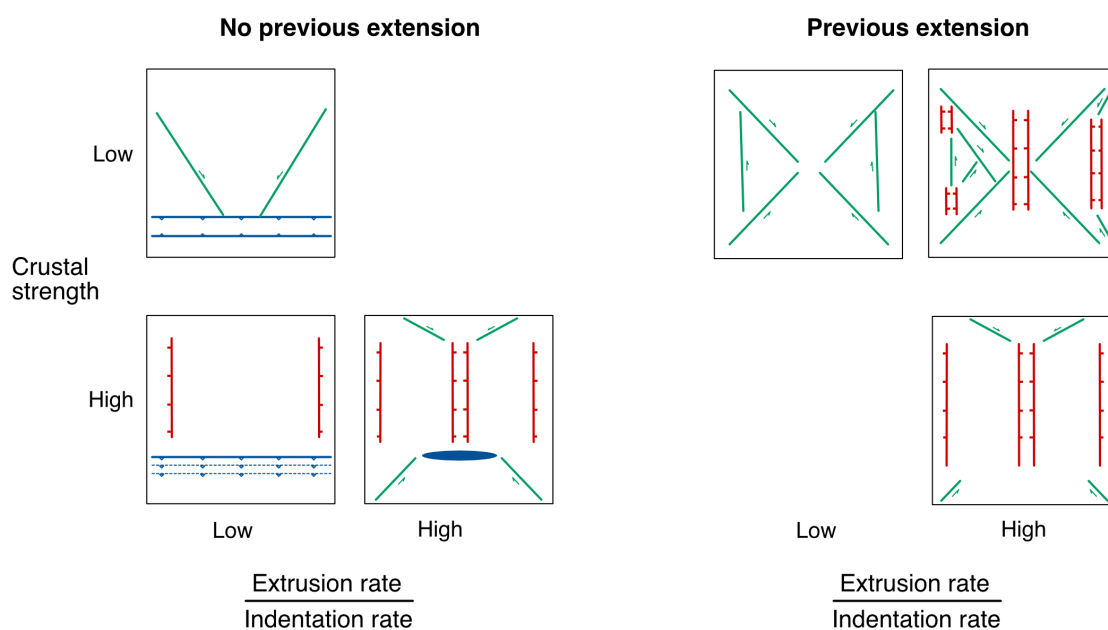
Figure 13. Synthesis of map view structures observed as a function of crustal strength, ratio of extrusion/indentation rates and tectonic inheritance. Thrust faults are in blue, strike-slip faults in green and normal faults in red.
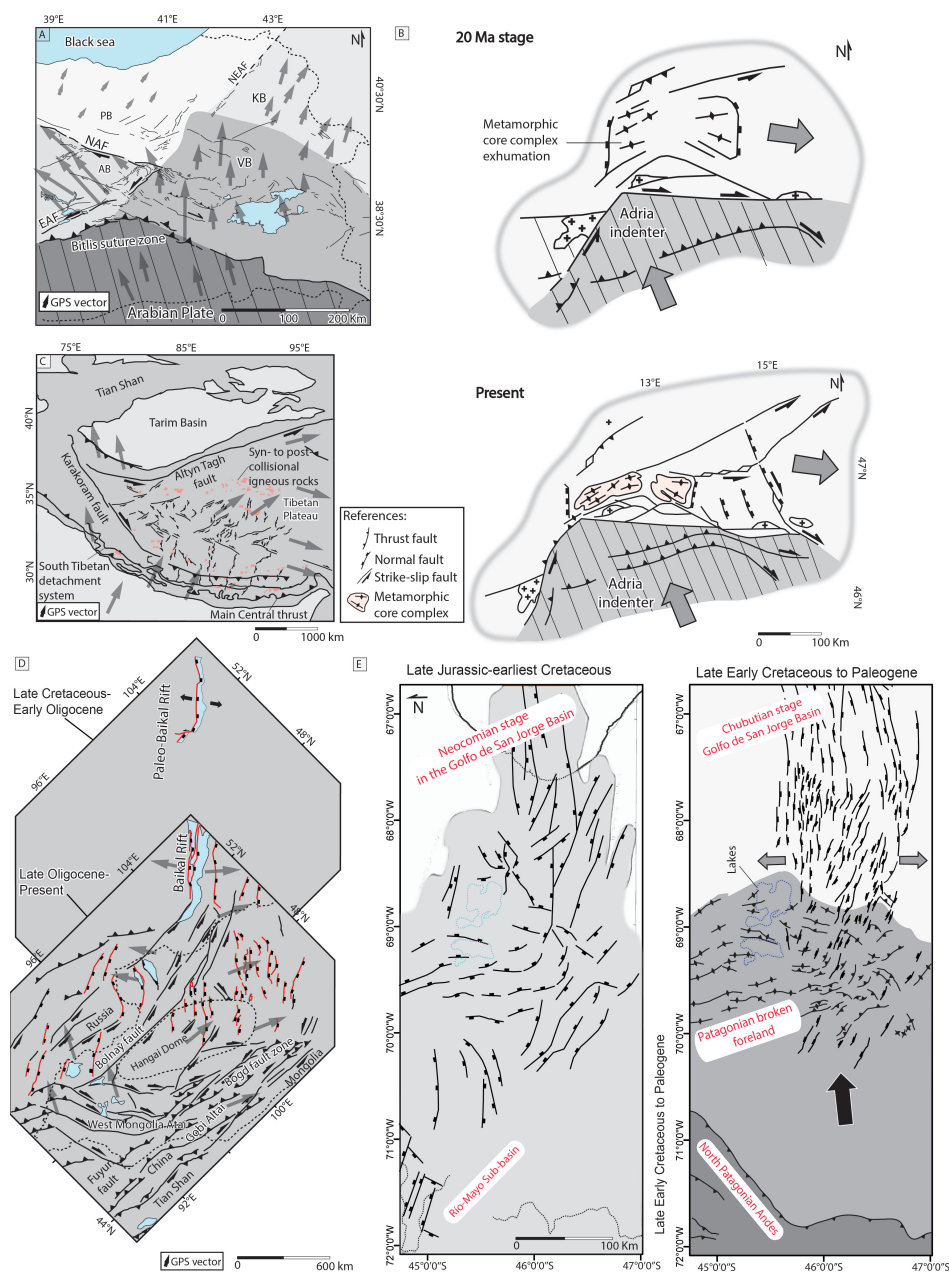
Figure 14. A) Structural map of the Eastern Anatolia region with GPS vector indicating crustal blocks kinematics. AB: Anatolide Block, KB: Kars Block, PB: Pontide Block, VB: Van Block, EAF: East Anatolian Fault, NAF: North Anatolian Fault, NEAF: North-East Anatolian Fault. Map modified from Hisarlı et al. (2016). B) Indentation and lateral extrusion in the Alps. 20 Ma stage: Onset of indentation, folding, and rapid extensional exhumation of thickening orogenic crust, fragmentation of wedge-shaped Austro alpine units south of the Tauern Window (basement complex). Present day stage: Oblique thrusting in Southern Alps, dextral strike-slip in northern Dinarides and eastward lateral crustal extrusion. Map modified from Scharf et al. (2013). C) Structural sketch map of the Tibetan plateau modified from Lu et al. (2018). D) Latest Cretaceous-Early Oligocene reconstruction of the Paleo-Baikal lake rift from Mats and Perepelova (2011) and a map of active structures in the Central Asia region from Yin (2010). E) Jurassic-Early Cretaceous extension and subsequent synorogenic foreland rifting reactivation stage of the late Early Cretaceous-Paleogene San Jorge Gulf Basin in Patagonia. Map modified from Gianni et al. (2015).

Table 1. Material properties.

Granular material: Fontainebleau Quartz sand	
Grain size range	$D_{50} = 210\ \mu$m
Density (specific)	2650 kg/m^3
Density (sieved)	1400 kg/m^3
Friction coefficient (peak)	0.74
Friction coefficient (reactivation)	0.64*-0.68**
Cohesion	60-70 Pa
Viscous material: PDMS	
Density	965 kg/m^3
Viscosity	3.5×10^4 Pa s
Rheology	Newtonian (n∼1)

* after 10 s; ** after 2.6h

Table 2. Scaling between the model and nature. By convention, ratios (*) are given as laboratory/nature.

Scaling	Experiment	Nature
Thickness (L)	0.04 m	15×10^3 m
Density (ρ)	1400 kg/m^3	2800 kg/m^3
Gravitational acceleration (g)	9.81 m/s^2	9.81 m/s^2
Viscosity (η)	3.5×10^4 Pa s	10^{21} Pa s
Stress $\sigma^* = \rho^* L^* g^*$	1.33×10^{-6}	
Strain rate $\dot{\epsilon}^* = \sigma^* / \eta^*$	3.8×10^{10}	
Time $t^* = 1/\dot{\epsilon}^*$	2.63×10^{-11}	
	1 h	*4.35 Ma*
Velocity $v^* = L^* / t^*$	1.01×10^5	
	40 mm/h	*3.46 mm/yr*